IOP Publishing Plasma Sources Science and Technology
Plasma Sources Sci. Technol. **26** (2017) 125004 (21pp) https://doi.org/10.1088/1361-6595/aa9304

Nanosecond surface dielectric barrier discharge in atmospheric pressure air: I. measurements and 2D modeling of morphology, propagation and hydrodynamic perturbations

Yifei Zhu[1], **Sergey Shcherbanev, Brian Baron and Svetlana Starikovskaia**[1]

Laboratory of Plasma Physics (CNRS, Ecole Polytechnique, UPMC, Univ. Paris-Sud, Observatoire de Paris, Paris-Saclay University, Sorbonne Universities), Ecole Polytechnique, route de Saclay, 91128 Palaiseau, France

E-mail: yifei.zhu@lpp.polytechnique.fr, sergey.shcherbanev@lpp.polytechnique.fr, Brian.baron@curie.fr and svetlana.starikovskaya@lpp.polytechnique.fr

Received 27 July 2017, revised 14 September 2017
Accepted for publication 12 October 2017
Published 16 November 2017

Abstract

A parallel 2D code for modeling nanosecond surface dielectric barrier discharge (nSDBD), combining a discharge description, detailed kinetics and hydrodynamics, is developed and validated. A series of experiments and numerical modeling for a single pulse nSDBD in atmospheric pressure air at a voltage amplitude of 24 kV have been performed. The measured and calculated velocity of the discharge front, electrical current, 2D map of N_2 ($C^3\Pi_u$) $\rightarrow$ $N_2(B^3\Pi_g)$ emission and hydrodynamic perturbations caused by the discharge on the time scale 0.2–5 μs are compared. The data are presented and analyzed for the negative and positive polarity of the streamers. A set of parametric calculations with different dielectric permittivities and different dielectric thicknesses is presented.

Keywords: nanosecond surface dielectric barrier discharge, modeling, measurements, nSDBD

1. Introduction

The special attention paid to surface dielectric barrier discharges (SDBD) over the last three decades is explained by their potential application for the active control of airflows. The dynamics of near-surface electric discharges and their interaction with the airflow is a subject of a recent review [1], in which the authors distinguish four types of flow perturbations: (1) low-speed near-surface gas motion generated by electrohydrodynamic interaction (ion–wind); (2) spanwise and streamwise vortices formed by both electrohydrodynamic and thermal effects; (3) weak shock waves produced by rapid energy release (fast gas heating) in pulsed nanosecond discharges; and (4) near-surface localized stochastic perturbations in sub-millisecond time.

High pressure nanosecond surface discharges in noble gases or in excimer mixtures (noble gases with the addition of reactive gases containing elements of group 17, such as fluorine or chlorine) were studied for laser applications in the 1970s and 1980s (see, for example, [2]). Pioneering experiments where nanosecond SDBD (nSDBD) in atmospheric air were used for flow control date to the beginning of the 21st century [3, 4]. Since then, an intensive study of nanosecond DBD actuators has been conducted by different groups [5–8]. It has been confirmed that the reason for the flow reattachment over a wide range of discharge pulse frequencies is the generation of thermal/pressure perturbations by nanosecond SDBD actuators.

[1] Authors to whom any correspondence should be addressed.

In spite of the fact that the principal reason for nSDBD discharge–flow interaction has been found and proved, the parameters of nSDBD plasma and the physics of the discharge are not yet clearly understood. The present work is the first of two papers. Part 1 describes the measurements and 2D modeling of an nSDBD, and the morphology, propagation of the discharge along the dielectric and hydrodynamic effects in the early afterglow are discussed. Part 2 presents the experimental and numerical study of plasma parameters in atmospheric pressure single shot nSDBD discharge.

Only a few well-established experimental facts regarding nanosecond discharges can be found in the literature. The morphology and dynamics of nSDBDs are usually measured by nanosecond ICCD imaging in the UV and visible range of spectra. The available data provide a top view above the dielectric [4], while the fine structure of the discharge in the direction perpendicular to the dielectric remains virtually unstudied. Only a few attempts to measure the distribution of emission in the direction from the dielectric to the bulk of the plasma [9, 10] exist in the literature. In [9], the surface barrier discharge is initiated over the ceramics or glass-ceramics by a 5–14 kHz sinusoidal voltage of 2.2–2.8 kV in amplitude. A segment corresponding to about 10 mm of the discharge along the dielectric was monitored using a photon counting technique. The conclusion was made that the thickness of the discharge is about 1 mm. In [10], cross-correlation spectroscopy was used to obtain a 2D picture of N_2 emission. The thickness of the emission layer did not exceed 1–2 mm. Because of the coplanar geometry of the electrodes in [10], the results cannot be directly compared to nSDBD in a classical airflow configuration.

A reduced electric field was derived in [11, 12] from the measurements of the ratio of emission of the first negative (1^-) and second positive (2^+) systems of molecular nitrogen—the technique developed for uniform plasma [13, 14]. The following conclusions were made on the basis of joint experimental and numerical analysis [12]: (i) the electric field in nSDBD is high but cannot be measured from the optical emission without special precautions; the emission of the 1^- and 2^+ systems comes from different spectral regions near the surface of the dielectric within a scale of tens of microns; (ii) to compare the experimentally measured ratio of emission and numerical modeling, it is necessary to integrate the results of the calculations in space, 'imitating' the light collection by the spectral system; (iii) a comparison of the experiments and numerical modeling provides similar values for the negative polarity nSDBD and different values for the positive polarity streamer: there is a region of a high electric field producing 'more emission' of the 1^- system in the experiments.

Recent measurements of the electric field above the water surface [15] should be mentioned since the developed technique can be adapted for nSDBDs. The field was measured by picosecond four-wave mixing in a 0.6 mm gap volume DBD in collinear phase-matching geometry using an absolute calibration provided by measurements of a known electrostatic electric field. The resolution of the technique is 0.2 ns, and the time resolution of the measurements was controlled by the jitter between the discharge pulse and the laser pulse, which was approximately 2 ns.

The SDBD excited by a single pulse of a few tens of nanoseconds is an efficient object to study the physics of surface DBDs, in particular, to compare the experimental data and results of numerical modeling. The discharge starts from the edge of the high-voltage electrode as a set of synchronous streamers—the delay between the streamers is less than 0.1 ns, and the propagation of the discharge along the non-charged surface simplifies the interpretation of the experimental data. Although in the experiments the nSDBD has a 3D structure, the synchronous motion of the streamers is the reason why, in numerical modeling, the nSDBD is represented by a 2D plasma layer. Modeling the nanosecond surface discharge demands significant computational efforts. It is complicated compared to the modeling of a volumetric streamer because a region with high gradients exists not only in the streamer head but also near the dielectric. Pioneering papers mainly considered electrohydrodynamic forces and aerodynamic flow acceleration in SDBD [16, 17] in air. Later, Gibalov and Pietsch [18] discussed numerical modeling in three possible configurations of barrier discharge—volumetric, coplanar and surface discharge arrangements—and provided a broad review of the available experimental data. The paper described the general peculiarities of cathode- and anode-directed streamers in any barrier discharge configuration.

Recent publications [19–22] describe the development and propagation of a nanosecond surface streamer. We believe that this is the most detailed and complete analysis of the physics of a nanosecond SDBD available at present. On the basis of the coupled solution of Poisson's equation, transport equations for charged particles, photoionization and a minimum set of kinetic equations for charged species, the propagation of the streamer initiated by a high-voltage nanosecond pulse has been studied. Different shapes of the discharge were reported: diffuse discharge for negative polarity, with a thin (a few microns) layer of a high electric field and low electron density in the vicinity of the dielectric, and a 'streamer–like' discharge for positive polarity—the thickness of the layer of the high electric field under the streamer is tens of microns. The specific energy distribution in the discharge was calculated on the basis of the current density and electric field. It was shown that in the negative polarity discharge, the energy is concentrated near the high-voltage electrode (cathode) whereas in the positive polarity streamer, the energy is spread almost uniformly along the streamer. This statement seems to contradict the experimentally observed pressure perturbations, producing similar shadow or Shlieren images at a typical time of a few microseconds [23].

Paper [24] presents a comparative numerical study of nSDBD discharge for both polarities for a high ($\varepsilon = 16$) value of a dielectric permittivity, with a voltage of 12 kV and a dielectric thickness of 0.5 mm. Calculations were performed using two different approaches. Calculations using a 2D fluid model were compared with the calculation using a new hybrid model. The hybrid model considered bulk electrons in a fluid approximation, while electron Monte Carlo simulation (EMCS) was used to treat energetic secondary electrons in a kinetic way. The calculation confirmed the qualitative behavior of the positive and

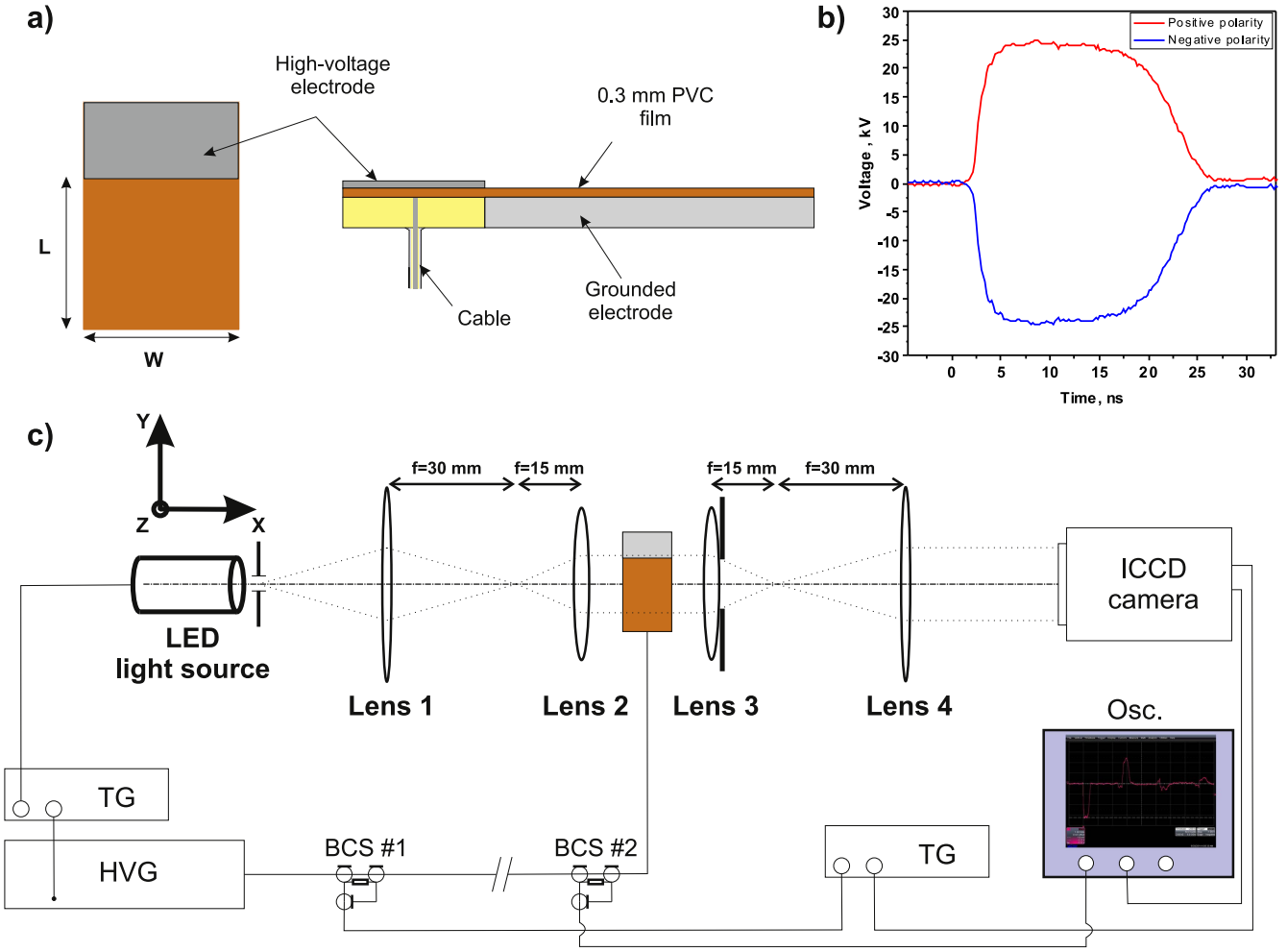

Figure 1. Experimental setup (a) electrode system; (b) profiles of applied voltages; (c) general scheme of the experiment. TG is a triggering generator, HVG is a high voltage generator, BCS is a back current shunt.

negative polarity streamers obtained earlier. A consistent set of velocities, isolines of the electron density, ionization source and electric field near the streamer head, has been presented. It was shown that the positive polarity streamer does not change when using the EMCS module. With a negative polarity applied to the high-voltage electrode, the anode layer is formed between the streamer body and the surface. The electrons are trapped in the sheath region by the electric field and produce a thin near-surface layer ahead of a streamer.

Linking together Poisson's equation, transport equations, the stiff system of detailed chemical kinetics and hydrodynamics is a challenging task for numerical modeling. For multi-scale modeling to be a practical predictive tool that is reasonably time-efficient requires highly optimized codes and parallelization of the calculations.

The aim of this work is to present together a parallel 2D code for modeling nSDBD, and a comparison of experiments and numerical modeling for the same experimental conditions. The measured and calculated velocities of the discharge front, electrical current, 2D map of N_2 $(C^3\Pi_u) \rightarrow N_2(B^3\Pi_g)$ emission, and hydrodynamic perturbations caused by the discharge on the time scale 0.2–5 μs are compared. The data are presented and analyzed for the negative and positive polarity of the streamers. A set of parametric calculations with different dielectric permittivities and different dielectric thicknesses is suggested.

2. Experimental setup and technique of measurements

A standard airflow configuration of the nSDBD [1] was used in the experiments. The electrode system is shown schematically in figure 1(a). The aluminium bar was 10 mm $\times$ W $\times$ L , where W is the width (or span) and L is the length of the ground electrode. The 0.3 mm thick PVC dielectric layer (dielectric permittivity $\varepsilon = 3.5$) was glued by a silicon glue ($\varepsilon \approx 3$) on the upper surface of the aluminium bar. The summary thickness of the dielectric layer was equal to 0.5 mm. For the high voltage electrode, a rectangular piece of copper foil 12 mm $\times$ W mm and 50 μm thick was glued on the PVC layer. The thickness of the conductive glue did not exceed 10 μm. The span of the electrode system, W, varied between 25 mm and 80 mm, and the length was taken to be constant and equal to $L = 80$ mm. The experiments were carried out in atmospheric pressure air at ambient temperature without gas flow.

Figure 1(a) presents a general scheme of the experimental setup. The electrode system was connected to a 30 m long coaxial cable. The high-voltage pulses of positive or negative polarity (20 ns duration at FWHM, 2 ns rise time and 10–30 kV amplitude) were transmitted from the high voltage generator (commercial FID Technology pulser, FPG20–03PM/NM) to the electrodes with a frequency of 2 Hz or lower. A back current shunt (BCS #1) installed with the electrode was used to synchronize the opening of the ICCD camera with a high voltage profile. A calibrated back current shunt (BCS #2) in the middle of the cable was used to measure the voltage on the high voltage electrode, the electric current and the deposited energy. Electrical signals were registered by a LeCroy WaveRunner 600 MHz oscilloscope. ICCD images of the discharges were taken with a Pi-Max4 Princeton Instruments ICCD camera with Edmund Optics 50 mm focus length objective.

Measurements by back current shunts are based on the fact that the voltage between the central wire and grounded shield is related to the electric current in the cable as $U = IZ$, where Z is the cable impedance. The velocity of the propagation of the electromagnetic signal in the cable is limited, $v_c = c/\sqrt{\varepsilon\mu}$, where c is the velocity of light in free space, ε and μ the dielectric permittivity and magnetic permeability of the media, respectively. The pulse coming from the high voltage generator (the incident pulse, U_{inc}) and the pulse reflected from the discharge cell (the reflected pulse, U_{refl}) are separated in time at the point where the back current shunt is situated. The value of the voltage on the electrode is equal to $U(t) = U_{\mathrm{inc}}(t) + U_{\mathrm{refl}}(t)$ at the conditions of DBDs, where the impedance of the load is much higher than the impedance of the cable, $U \approx 2U_{\mathrm{inc}}$. The waveform of the voltage on the high voltage electrode is given in figure 1(b). (For further details, the back current shunt technique can be found elsewhere [25, 26].)

To study the microstructure of the discharge, shadowgraph images and optical emission images were obtained using an optical system where a system of quartz lenses, presented in figure 1(c), was used instead of the objective of the ICCD. A Thorlabs green LED M505L3-C with a 505 nm central wavelength and 30 nm bandwidth was used as a light source. To increase the intensity of the background light, the LED was powered by a custom-made pulsed source, the pulse duration being 15 μs. A symmetric system of lenses provided a uniform light beam from the LED and 2× magnified image of the discharge. A diaphragm 5 mm in diameter was installed after lens 3; although the intensity of the light decreased, the increased depth of field significantly exceeded the length of the high-voltage electrode, so the distortions of the emission caused by the presence of adjacent streamers were minimized. A camera was placed at the 2D translation platform. A Γ-shape mask from the copper foil (20 μs in thickness) was used: (i) to check the depth of field; and (ii) to ensure that the electrode system was perpendicular to the axis of the optical diagnostic system. The spatial resolution of the system was equal to 6.4 μm/pixel at an ICCD camera gate equal to 0.5 ns; the jitter was less than 0.1 ns.

3. Numerical approach

A 2D parallel PASSKEy ('PArallel Streamer Solver with KinEtics') code coupling plasma and hydrodynamics has been developed to model nSDBD development. The computational model is a 2D self-consistent description of a multi-species mixture under the action of discharge and hydrodynamic expansion in the early afterglow, with detailed chemical kinetics and energy release in chemical reactions. The code is optimized using a hybrid OpenMP–MPI parallel approach.

3.1. Governing equations

The continuity equations combined with the Poisson's equation and discharge/afterglow chemical kinetics were solved to describe the behavior of charged, neutral, excited species and the electric field. The continuity equations for the species are

$$\frac{\partial n}{\partial t} + \nabla \cdot \boldsymbol{j} = S + S_{\mathrm{ph}} \tag{1}$$

where n is the number density of the species of interest, $\boldsymbol{j}$ is the flux of species, S is the source term of the species due to chemical reactions, and S_{ph} is the source term due to photoionization. Based on drift–diffusion approximation, the flux term $\boldsymbol{j}$ can be expressed as

$$\boldsymbol{j} = \mu n \boldsymbol{E} - D\nabla n \tag{2}$$

where D, μ are the diffusion coefficient and mobility of the charged species, and $\boldsymbol{E}$ is the electric field. In the code, $\nabla \cdot \boldsymbol{j} = 0$ for neutral species was postulated.

The chemical source term S is described by detailed kinetics in the code. The kinetics scheme in [27], suggested by Pancheshnyi to model streamer propagation, and part of [28] suggested by Popov to describe fast gas heating, were combined and used. The following neutral, charged and excited species are taken into account: e, N_2, $N_2(A^3\Sigma_u^+)$, $N_2(B^3\Pi_g)$, $N_2(C^3\Pi_u)$, N_2^+, N_4^+, O_2, O, $O(^1D)$, O_2^+, O^-, O_2^-. The scheme includes 13 species and 38 reactions.

The photoionization model [29] describing the ionization of oxygen molecules by VUV-radiation coming from electronically-excited N_2 in $b^1\Pi_u$, $b'^1\Sigma_u^+$, $c'^1_4\Sigma_u^+$ states is considered. The model is based on the assumption that the major contribution to the rate of photoionization comes from the radiation in the spectral range 98–102.5 nm; the radiation below 98 nm is absorbed by molecular nitrogen, and the wavelength 102.5 nm is the photoionization threshold of O_2. The photoionization source term S_{ph} is calculated by introducing three-term Helmholtz equations [30, 31]:

$$S_{\mathrm{ph}} = \sum_j S_{\mathrm{ph}}^j, \tag{3}$$

$$\nabla^2 S_{\mathrm{ph}}^j - (\lambda_j p_{O_2})^2 S_{\mathrm{ph}}^j = -A_j p_{O_2}^2 I, \tag{4}$$

$$I = \xi \frac{p_q}{p + p_q} \alpha \mu E n_e, \tag{5}$$

where α is the Townsend ionization coefficient, μE is the absolute drift velocity of electrons, p is the ambient pressure, p_q is a quenching pressure of $C^3\Pi_u$, p_{O_2} is a partial pressure of O_2. λ_j and A_j are fitting coefficients for photo-ionization functions obtained in experiments and taken from [30]. Quenching pressure is expressed as $p_q = kT/\tau_0 k_q$, where k is the Boltzmann constant, T is the gas temperature, τ_0 and k_q are the radiative lifetime of the transition and the rate constant of collisional quenching respectively.

Poisson's equation is solved taking into account different values of dielectric permittivity:

$$\nabla \cdot (-\varepsilon_0 \varepsilon \nabla \phi) = q_e \sum_i Z_i n_i \tag{6}$$

where q_e is the absolute value of electron charge, ε_0 is the permittivity of free space and ε is relative permittivity. Z_i is the charge of species i, and n_i the number density of species i.

Finally, the system of equations is closed with Euler equations:

$$\frac{\partial \boldsymbol{U}}{\partial t} + \frac{\partial \boldsymbol{F}}{\partial x} + \frac{\partial \boldsymbol{G}}{\partial y} = \boldsymbol{S} \tag{7}$$

$$\boldsymbol{U} = \begin{bmatrix} \rho \\ \rho u \\ \rho v \\ e \end{bmatrix}, \boldsymbol{F} = \begin{bmatrix} \rho \\ p + \rho uu \\ \rho uv \\ (e + p)u \end{bmatrix}, \boldsymbol{G} = \begin{bmatrix} \rho v \\ \rho uv \\ p + \rho vv \\ (e + p)v \end{bmatrix}, \boldsymbol{S} = \begin{bmatrix} 0 \\ 0 \\ 0 \\ S_{heat} \end{bmatrix} \tag{8}$$

where ρ is the total density of air, u and v are the velocities in two dimensions, and e is the specific total energy. The reactive Euler equations are closed by the equation of state:

$$p = (\gamma - 1)\rho i \tag{9}$$

where $i = e - (u^2 + v^2)/2$ is the specific internal energy.

The energy, released in fast gas heating and calculated from kinetic equations in plasma code, is used as a source term in equation (8). The calculated density, pressure and temperature from the Euler equations are further used for E/N calculation, Helmholtz equations and kinetics.

3.2. Numerical schemes

Poisson's equation and Helmholtz equations are solved by a preconditioned conjugate-gradient solver [32, 33]. A semi-implicit time integration scheme was used for Poisson's equation to release the limit of the dielectric relaxation time [34, 35]. For the transport equations, a 1st order splitting method is used for time integeration:

$$V^{t+\Delta t} = C^{\Delta t} D^{\Delta t} R^{\Delta t} V^t \tag{10}$$

where $V^{t+\Delta t}$ and V^t are the solution of equation (1) at t and $t + \Delta t$, respectively. $C^{\Delta t}$, $D^{\Delta t}$ and $R^{\Delta t}$ represent the drift (convection), diffusion and chemistry operator respectively applied on the duration Δt. Different schemes are used for each operator. For the drift term, an explicit UNO3 scheme (3rd order in time and space) [36] coupled with the Strang operator for spatial splitting is used. For diffusion, an explicit 2nd order central discretization scheme is used, while for chemistry, the stabilized Rouge–Kutta–Chebyshev scheme [37] is used.

Euler equations are calculated at every iteration after solving the plasma equations. The updated neutral densities, temperature and reduced electric field are used in the next iteration for plasma calculations. The Z/B flux vector splitting scheme [38] is used to capture strong spatial discontinuities of solutions during simulation.

Table 1. Boundary conditions for transport equations of species.

Boundary condition	Flow towards boundary	Flow away from boundary
Electrons	$\partial \boldsymbol{j_e}/\partial n = 0$	$\boldsymbol{j_e} = -\gamma \boldsymbol{j_i}$
Ions	$\partial \boldsymbol{j_i}/\partial n = 0$	$\boldsymbol{j_i} = 0$

3.3. Initial and boundary conditions

To ignite the discharge, an initial cloud of seed plasma was chosen according to the electric field from the very beginning of the start time. In this calculation, the voltage (the 24 kV waveform shown in figure 1(b)) starts from 1.5 kV instead of 0 kV to pass the non-important and time-consuming voltage increase and non-discharge period. With this initial voltage, we calculated the electric field, giving the range of the region where ionization starts ($E > 32$ kV cm^{-1}), and then distributed seed plasma in this region by following formula 11 (in cm^{-3} and cm):

$$\begin{aligned} n_e(x, y) &= n_i(x, y) \\ &= 10^{12} \exp(-(x/0.002)^2 - (y/0.002)^2)). \end{aligned} \tag{11}$$

Several numerical tests have validated that the range of this Gaussian peak value from 10^9–10^{13} cm^{-3} does not affect the propagation of the surface streamer after 0.1 ns.

For Poisson's equation, classical Dirichlet boundary conditions were used for the metal surfaces, $\phi = U(t)$. Newmann boundary conditions were written for the non-metal boundaries, $\partial\phi/\partial n = 0$. Surface charge is accumulated on the dielectric surface during each time step by collecting the charge flux flowing towards the dielectric on the boundary of the plasma region. The accumulated charge is then stored in the edge of the finite volume mesh cell, and was taken into account as additional charge when solving Poisson's equation. For the Helmholtz equations, $S_{ph} = 0$ was set on the boundary of the domain (far from the plasma region).

For transport equations, the boundary conditions are summarized in table 1. It has to be noted that we assume the secondary emission coefficient on both the metal and dielectric, $\gamma = 0$, as calculations carried out have shown that the results do not visibly depend on γ ranging from 0.01–0.1.

For Euler equations, classical non-slip wall boundary conditions were given to the entire calculation domain; the flux is given as:

$$\boldsymbol{Z_w} = \begin{bmatrix} 0 & p & p & 0 \end{bmatrix}. \tag{12}$$

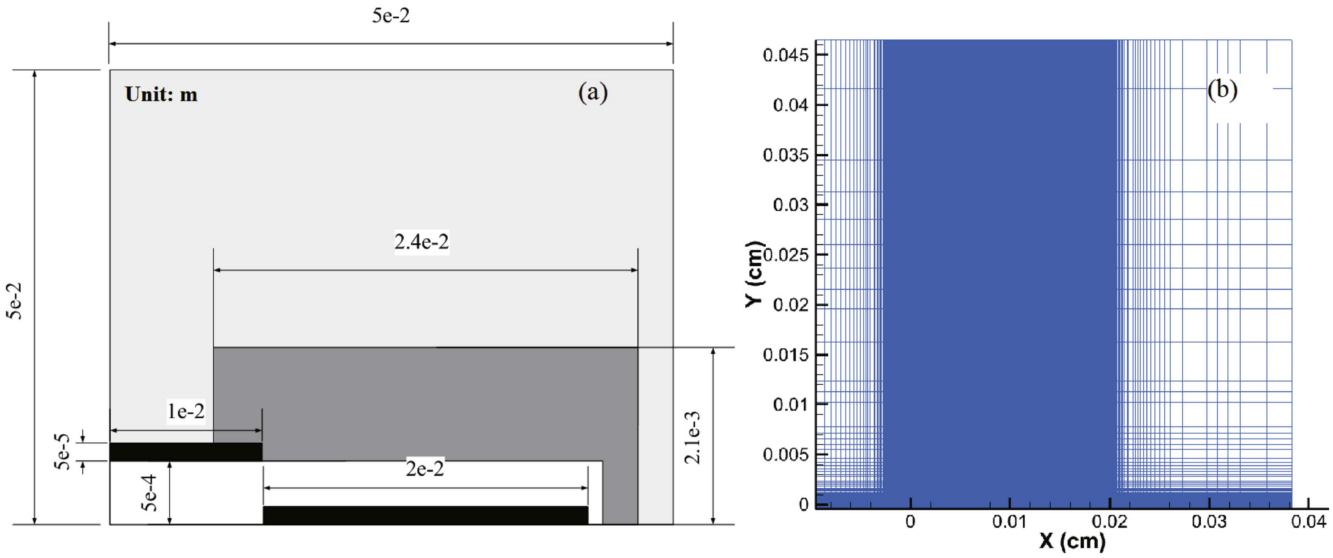

Figure 2. Computational domain and mesh distribution (units are in meters) (a) computational domain for different equations. Transport equations: dark grey domain; Poisson's equation and Helmholtz equation: entire domain; Euler equations: light and dark grey domain; (b) structured cartesian mesh, uniform square mesh with a size of 5–8 μm in the dark grey domain exponentially growing in the rest of the computational domain.

3.4. Domain, mesh, timesteps and parallelization

A total computational domain of 5 cm × 5 cm is shown in figure 2(a). To reduce the computational cost, the transport equations, Poisson's equation, Helmholtz equations, and Euler equations were solved in different sub-domains. A fine and uniform square mesh was distributed in the streamer propagation region, while in the rest of the computational domain, the mesh size grew exponentially, as can be seen in figure 2(b).

All grids were integrated simultaneously with the same time step, which is limited by different characteristic time steps [39], including the drift dynamics time step $\Delta t_c = \min\left[\frac{\Delta x_i}{v_{x(i,j)}}, \frac{\Delta y_j}{v_{y(i,j)}}\right]$, the diffusion dynamics time step $\Delta t_d = \min\left[\frac{(\Delta x_i)^2}{D_{x(i,j)}}, \frac{(\Delta y_j)^2}{D_{y(i,j)}}\right]$, the kinetics time step $\Delta t_I = \min\left[\frac{n_{k(i,j)}}{S_{(i,j)}}\right]$ and the dielectric relaxation time step, $\Delta t_{Diel} = \min\left[\frac{\varepsilon_0}{q_e \mu_{e(i,j)} n_{e(i,j)}}\right]$. The limit from the dielectric relaxation time step is removed due to the use of a semi-implicit scheme for Poisson's equation. Thus, the general time step Δt was defined as:

$$\Delta t = \min\left(\xi_c \Delta t_c, \xi_d \Delta t_d, \xi_I \Delta t_I\right) \tag{13}$$

where $\xi_c = 0.1$, $\xi_d = 0.1$ and $\xi_I = 0.02$.

Despite the removal of the dielectric relaxation time limit, the time step during calculation is still very small due to the high reaction rates, and the computation cost grows significantly with an increase in the kinetics dimension.

To accelerate the calculation, an OpenMP–MPI hybrid approach was developed in this work, with OpenMP parallelization operated on 16 CPU cores to perform time integration of the transport equations and to perform LU factorization and iterations for the Poisson and Helmholtz equations, while MPI parallelization operated on different nodes according to the dimension of the kinetics scheme. The suggested hybrid approach combines the advantages of both the OpenMP method and MPI techniques, and avoids the drawbacks of intense and time consuming message exchange between different nodes in pure MPI codes.

The calculation time depends mainly on the scale of the mesh and kinetics. For 10^6 cells and 38 kinetic reactions, the calculation of a 2 cm surface streamer propagating under a voltage pulse of about 24 kV in amplitude takes 8–20 h on a single HPC node (Intel Xeon E5, 2.40 GHz, 16 cores).

4. Code validation

A few benchmark cases of atmospheric pressure discharges were selected, namely a case of a volumetric streamer propagation in point-to-plane geometry with minimized discharge kinetics containing ionization and attachment [40], streamer development taking into account detailed chemical kinetics [27], the development of a nanosecond discharge at high overvoltage [41], and SDBD [12, 22, 24]. For all selected cases, the main results are correctly reproduced by the developed code. Two examples, for volumetric [40] and for surface [12, 22] streamers, are presented below.

4.1. Streamer in point-to-plane geometry

Paper [40] is a classical study of streamer propagation. The calculations [40] were conducted for a hyperboloid anode placed 1 cm over a plane cathode in atmospheric pressure air. A constant voltage of 13 kV was applied to the anode. The rate of collisional ionization was calculated in the approximation of the local electric field, $S_i = \mu E \alpha n_e$, where α is the first Townsend ionization coefficient. Two-body dissociative

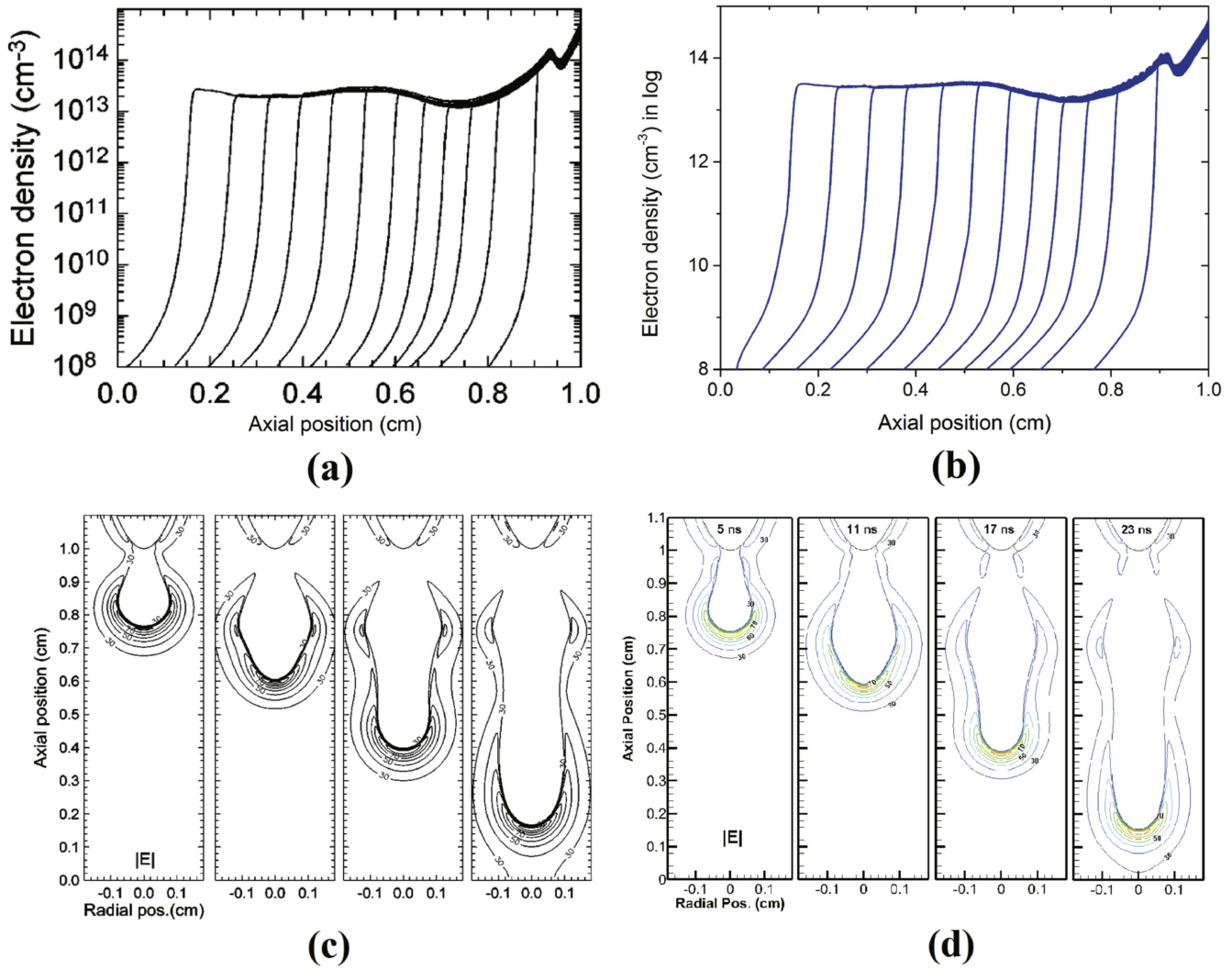

Figure 3. Validation of PASSKEy code developed in the present work on the benchmark case describing the volumetric streamer. (a), (b) Axial profiles of the electron density [40]. Time moments are 1–23 ns, step is 2 ns, the streamer propagates towards $z = 0$ (a) results of [40]; (b) PASSKEy code; (c), (d) contour lines of absolute values of the electric field, in logarithmic scale, time moments are 5, 11, 17, and 23 ns. The contours are 30, 40, ... kV cm^{-1}. (c) Results of [40]; (d) PASSKEy code.

attachment and three-body attachment of electrons to oxygen molecules were taken into account. Electron mobility, the diffusion coefficient, Townsend coefficient, and the reactions between charged particles were taken to be the same as in [40] with the aim of reproducing the calculations. Similar to [40], a small plasma spot was placed at the anode tip to initiate streamer formation.

Figure 3 compares the results of the calculation of the present work with the reference results taken from [40]. Calculated in the present work, axial profiles of the electron density and isolines of the electric field are shown in figures 3(b) and (d) respectively. Different computational approaches to photoionization have been used in [40] and in the present work. Both codes use the classical photoionization model developed by Zheleznyak *et al* [29]. In [40], the photoionization was calculated by integration over the region containing the emission sources; the region was a restricted volume related to the streamer head. The present work uses a three-exponential Helmholtz model summarized in [30] specifically for photoionization in air. Despite the described difference, the results calculated by the PASSKEy code provide good agreement with [40] (see figures 3(a) and (c)). The streamer is initiated in a high Laplacian field close to the anode and expands along the axis of the discharge and in the radial direction until it reaches a radius of approximately 1 mm. After this, the streamer propagates along the axis of the discharge gap with an almost constant radius of the channel and virtually constant velocity.

4.2. Surface streamer

Additional validation of the PASSKEy code was based on the calculations of the nanosecond surface discharge at atmospheric pressure. Numerous simulations of the surface streamers with rather different numerical approaches and configurations are known [12, 18, 22, 24, 42, 43]. Currently,

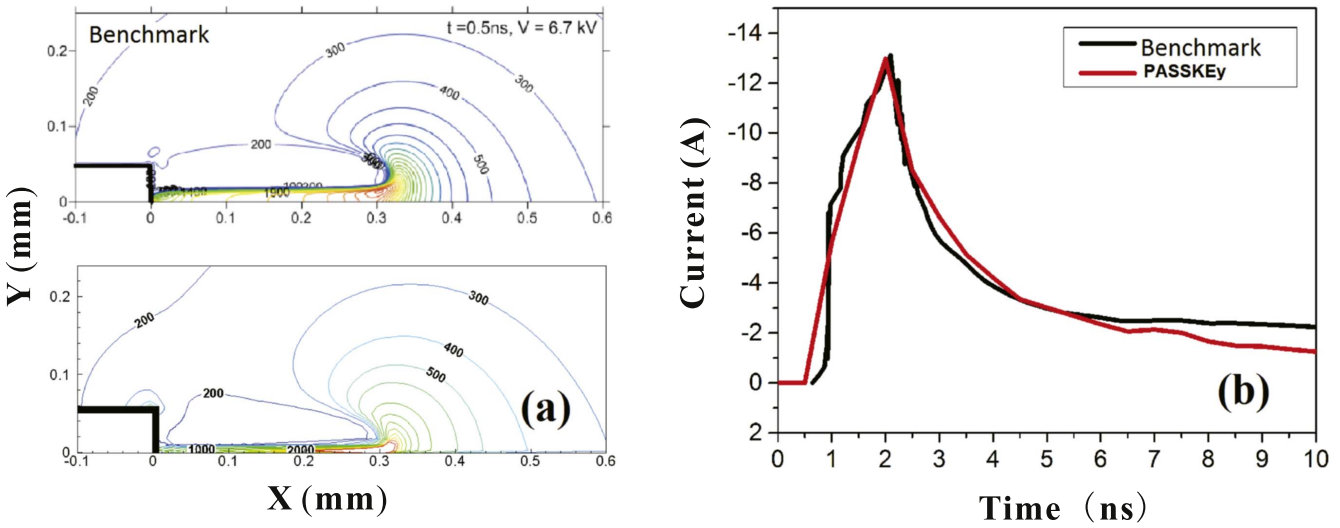

Figure 4. Validation of the PASSKEy code developed in the present work on the benchmark case describing the surface streamer (a) contour lines of the electric field at first 0.5 ns (Td) [12]; (b) electrical current through the high-voltage electrode [22].

there is no 'classical' benchmark for the case of an atmospheric pressure surface streamer. In this work, [12, 22] were selected for comparison.

Using the same geometry and voltage waveform, a 2D map of the absolute values of the electric field and the dependence of the electrical current upon time were calculated. They are shown in figure 4, together with the results taken from [12, 22]. The surface streamer starts from the edge of the high-voltage electrode, near the triple point (a junction point of the metal, dielectric and air), and propagates along the dielectric surface. With the enhanced electric field at the ionization head, the propagation velocity of the surface streamer is much higher than the volumetric streamer.

There are two principal differences in the model developed in [12, 22] and in the present work. A detailed description of the approach [12, 22] can be found in earlier papers [19]. The photoionization in [12, 22] uses model [29] and is calculated as the integral over the region of interest. The kinetic model used in [12, 22] is restricted by reactions of ionization for O_2 and N_2, recombination, dissociative recombination and detachment. The PASSKEy code uses the three-exponential Helmholtz model for photo-ionization [30]. The kinetic model contains 38 reactions, including the main set of reactions [12, 22] but also considering the reactions responsible for a fast energy release (fast gas heating) in reactions with charged and excited species.

It has to be noted that another difference between these two models is the treatment of the flux boundary condition of the dielectric. The boundary condition used in PASSKEy is given in table 1, which is quite classical and widely used for the plasma–dielectric interface in many groups [24, 42, 44, 45]. The boundary condition of the benchmark case is more sophisticated and specialized; an additional boundary flux term concerning thermal flux for electrons based on phenomenological estimations of elementary kinetics was introduced. As a result, when the electric field is negative in the Y direction over the dielectric, the electron flux flowing away from the dielectric surface will be reduced and the charge separation will be weaker, leading to a slightly thicker region between the streamer body and the dielectric.

In spite of the described differences between the PASSKEy code and the model presented in [12, 22], the results give a very good agreement for the streamer morphology and dynamics. The values of the electric field are similar at similar positions, and the electrical current through the high-voltage electrode is identical, indicating that the flux of species and the electric field near the boundaries are calculated correctly.

5. Results and discussion

Typical time-resolved ICCD images of the nSDBD discharge taken with the 1 ns ICCD gate are presented in figure 5. Here and elsewhere, the ICCD images are taken without any spectral selection of emission within the spectral range 300–800 nm. The camera sensitivity is the same for all the results presented in the figure. According to the current knowledge of nSDBDs, the optical emission in the mentioned range corresponds mainly to the second positive system of the emission of molecular nitrogen, $N_2(C^3\Pi_u) \rightarrow N_2(B^3\Pi_g)$ transition. The quenching time of $N_2(C^3\Pi_u)$ is determined by the collision with molecular oxygen, the rate constant being equal [46] to $k_Q^{O_2} = 2.7 \cdot 10^{-10}$ cm^{-3} s^{-1}. The efficient life time of $N_2(C^3\Pi_u)$ is 0.7 ns at atmospheric pressure, thus ICCD imaging adequately reflects the spatial structure of the discharge, and the resolution is limited by the camera gate. Two peaks of emission are observed during the development of the discharge (we will also use the terms 'the first stroke' and 'the second stroke', similar to [22])—one corresponding to the ionization wave charging the surface, on the rising front of the voltage pulse, and another, corresponding to the removal of the electrical charge from the surface on the trailing edge.

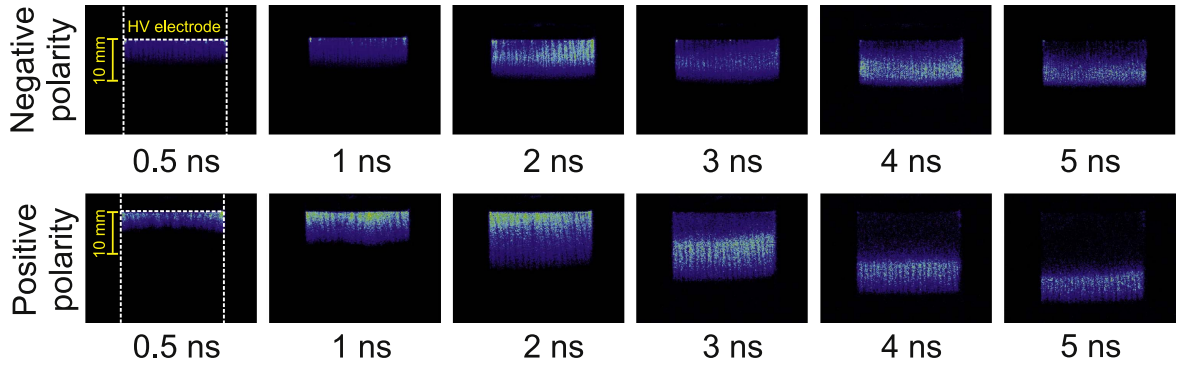

Figure 5. Typical time-resolved ICCD images of the nSDBD discharge (top view) of the negative and positive polarities of the applied pulse. The width of the high-voltage electrode (a span of the system) is $W = 25$ mm. The camera gate is 1 ns, and the time delay is indicated under each frame. Single-shot images without accumulation of the signal.

5.1. Measurements and modeling of streamer velocity and electric current

Similar ICCD images are usually used to plot the $x-t$ diagrams, presenting subsequent discharge front positions at different time instants, and to calculate the nSDBD propagation velocity. A few $x-t$ diagrams are shown in figure 6(a). The experiments were carried out in airflow geometry in quiescent ambient pressure air for the same high voltage pulse with amplitude $U = \pm 24$ kV. The shape of the pulse is presented by a dashed line in figure 6. The length of the grounded electrode, $L = 80$ mm, was always longer than the maximum length of the discharge propagation. The span of the electrode system (the length of the high voltage electrode) changed from $W = 25$ mm to $W = 80$ mm. For the 50 mm span, the data are presented for both the rising front and the trailing edge. Two waves of emission, corresponding to two ionization fronts, are clearly seen (indicated as I and II in the figure).

The first ionization front (the first stroke) propagates differently for negative and positive polarities of the high-voltage electrode: the velocity is significantly lower for the negative polarity discharge. The second ionization front (the second stroke) propagates with a similar velocity for both polarities. The maximal length of the propagation of the discharge L_{max} along the grounded electrode decreases with the length (span) of the high-voltage electrode, W. This effect is significant when passing from the 25–50 mm HV electrode (the transition is indicated with arrows in figure 6(a)), but then the maximal propagation length changes slowly with the HV electrode length, approaching to some asymptotic value. The $x-t$ diagram for the 50 mm span and 80 mm span are quite similar. The $x-t$ diagram obtained for the 63 mm long HV electrode in the coaxial system similar to the system described in [47] is in good correlation with the data obtained for the airflow electrode configuration. To plot the $x-t$ diagrams from the numerical results calculated by the PASSKEy code, the position of the front of the discharge was selected as a position of the front of the electron density. It can be clearly seen that the results of the numerical calculations are in excellent agreement with the experimental data for $W = 50$ mm and for longer HV electrodes.

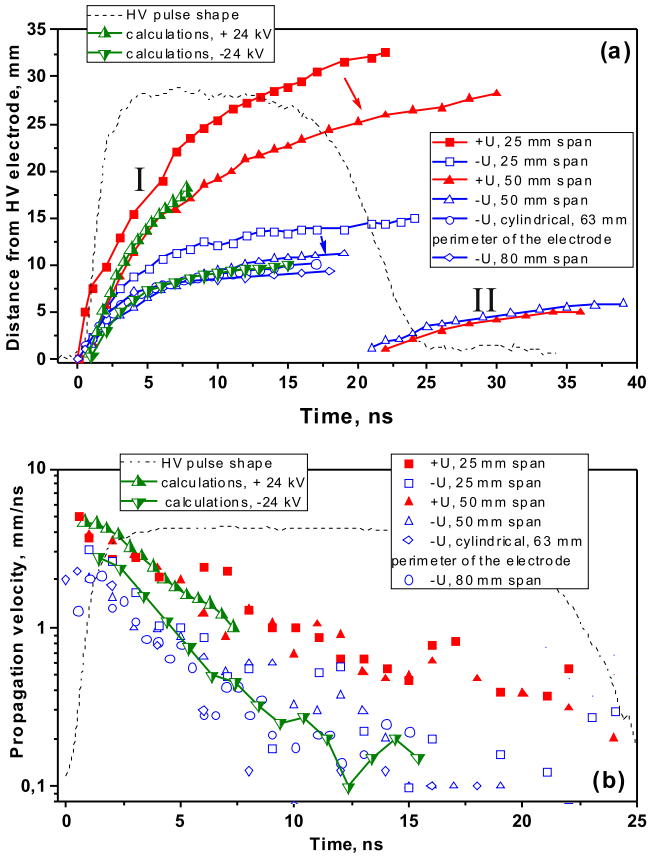

Figure 6. Experimentally obtained and calculated dynamics of the nSDBD propagation. (a) $x-t$ diagrams. I and II show the first and second ionization fronts, and the waveform of the voltage pulse is given by a dashed line; (b) velocity of the discharge front as a function of time. The synchronization with the data shape of the high-voltage pulse (a.u.) is indicated with a dashed line. Filled symbols represent positive polarity discharge; open symbols represent negative polarity discharge. Half-filled triangles represent numerical modeling. Data for different spans of the electrode system are marked by different symbols (see the legend).

The instantaneous speed of the discharge front was calculated for all time intervals of the first stroke presented on the $x-t$ diagram. The results are shown in figure 6(b). The experimental data are given by the hollow symbols for negative polarity and by the filled symbols for positive

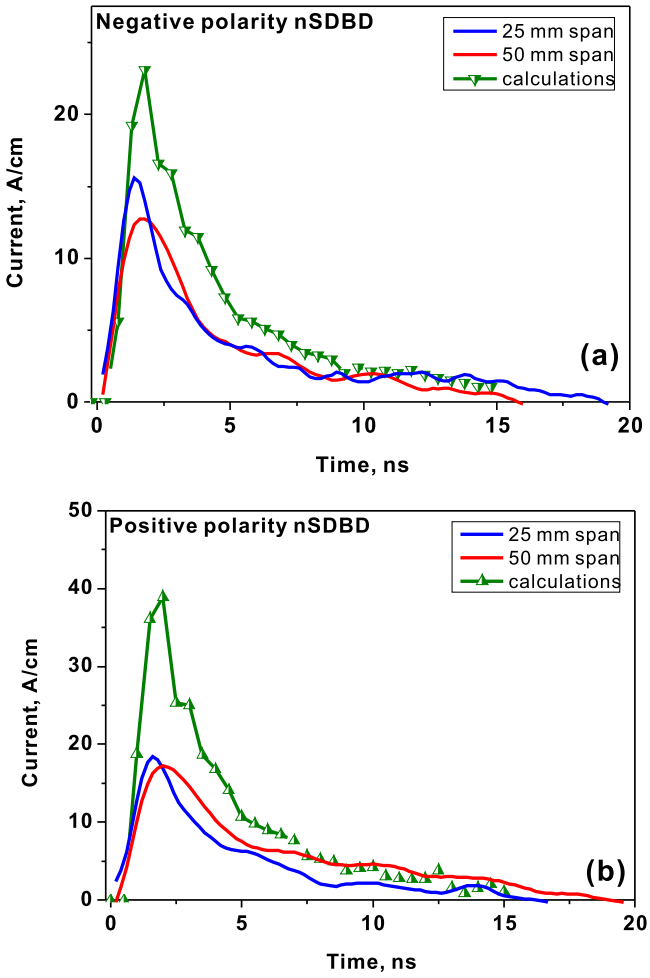

Figure 7. Discharge electrical current per unit length for negative (a) and positive (b) polarity nSDBD. The current was measured for two spans of the electrode system, $W = 25$ mm and $W = 50$ mm. The half-filled triangles represent the numerical modeling.

polarity. The half-filled symbols represent the results of numerical modeling. A quantitative agreement between the experimental data and calculations for both polarities is evident. It should be noted that in the calculations, the few first points were omitted: at the early stage of the discharge the velocity increases, reaches the maximum, and only the right branch of the velocity versus time was taken into account. No maximum velocity is observed experimentally. The reasons will be discussed in the final section (figure 14).

The velocity of the negative polarity streamer is systematically lower than the velocity of the positive polarity streamer. The velocity is about 2–3 mm ns^{-1} for negative and ~5 mm ns^{-1} for positive discharge at the early stage of propagation. It drops down to 0.1 mm ns^{-1} and less for the negative polarity streamer, while the positive polarity streamer continues to propagate with a velocity progressively decaying to 0.4–0.5 mm ns^{-1} at the end of the pulse.

This behavior is dictated by the difference in mechanisms of the negative and positive polarity streamers, described in a number of publications [12, 19, 22, 24]. The head of the surface streamer and the nearest region behind the head represent a complex structure combining the features of the volumetric streamers (photoionization and ionization by electron impact) and the presence of the dielectric surface (charge deposition on the dielectric with consequent enhancement of the electric field near the surface). When the length of the surface streamer exceeds a few millimeters, the head and the 'channel' are clearly distinguished. We will use the term 'channel' to designate a structure of the surface streamer behind the head, although for negative polarity, the electric field in this region is rather diffuse. For both polarities, there is a narrow region of high electric fields near the dielectric. For negative polarity streamers, it is reported to be a few micrometers, while for positive polarity, it comprises tens of micrometers [12, 20]. So, the channel consists of a thin zone of a very high electric field and low electron density and of the 'body' of the channel, described by contours of the electron density.

The principal difference in propagation is explained by the structure of the streamer head [12]. In the negative polarity streamer, the electrons produced in the cathode layer near the high-voltage electrode move to the surface, producing a negative charge surplus; finally, the electron density and the electric fields 'stick' to the surface compared to the positive polarity discharge. In the positive polarity discharge, on the contrary, the electrons go from the surface, and the ions virtually do not move. As a result, the structure of the field and the electron density pattern is different—the electric fields in and below the streamer head are very high and the propagation of the positive streamer is faster. Another important point is that the conductivity of the negative polarity streamer is lower. The drop of potential along the O–X axis consists of a near electrode drop (cathode or anode fall), a potential drop along the channel and a potential drop in the streamer head. A lower conductivity of the channel of the negative streamer results in a higher longitudinal electric field in the channel, a lower electric field in the head and, consequently, lower propagation velocity.

The described difference is clearly illustrated in [24] where the ionization sources, electron densities, and electric field in the vicinity of the streamer head of negative and positive polarity are calculated.

A simple estimate made in [47] for a negative polarity streamer was based on the idea that when the streamer stops, the electric field in the streamer head is close to zero. Assuming that the voltage on the cathode layer [48] is small compared to the potential of the cathode, it is possible to calculate the reduced electric field $(E/N)_{ch}$ in the channel of the negative polarity streamer. For $U = -24$ kV and for $L_{max} \approx 10$ mm, at $P = 1$ bar and $T = 300$ K, the value $(E/N)_{ch} \approx 100$ Td. When the positive polarity streamer propagates at much longer distances, it is reasonable to assume that the longitudinal electric field in the streamer 'body' is lower than in the case of the negative polarity discharge.

To analyze the influence of possible edge effects, the experiments with two different spans were selected to measure the electrical current: $W = 25$ mm and $W = 50$ mm. Figure 7 presents the experimentally measured total electrical

current through the discharge divided by the span of the electrode system and numerical results for the current per unit length. It is important to note that the electrical current corresponding to the charging of the electrode system in the absence of the discharge was subtracted when treating the data. In the numerical modeling, the current was calculated as an integral of fluxes of negative and positive charges through the surface of the high-voltage electrode.

The agreement is rather qualitative for both polarities. For discharge of negative polarity (figure 7(a)), the current peaks at 16 A/cm for the 25 mm span, and at 13 A/cm for the 50 mm span. The result obtained by numerical modeling for the same conditions is 25 A/cm, with the secondary emission coefficient on the electrode being $\gamma = 0.1$ and ion mobility ranging between 1.4 and 2.5 $cm^2/V{\cdot}s$ according to [49]. For the discharge of positive polarity (figure 7(b)), the current through the electrode is mainly the current of electrons; experiments give almost the same peak current value for 25 mm and 50 mm span, 18 A/cm and 19 A/cm. The result in the numerical simulation gives a two times higher peak current value in the first 5 ns (40 A/cm), and a decaying current that behaves similarly to the experimental ones.

Despite the difference in the peak current values, a good agreement is observed for the measured and calculated absolute values of the current after the peak; qualitative behaviour of the current as a function of time is also well reproduced. A detailed description of the shape of the pulse of the current linked to the phases of the development of the negative polarity discharge can be found in [22]. According to [22], the first peak of the current (20–40 A/cm in figure 7(a)) is due to the ion current from the cathode layer to the HV electrode. High electron densities and a high electric field result in strong charge separation [22] and a sharp rise of the current. The electrons produced in the cathode layer drift to the dielectric surface and charge the surface negatively. As a result, the *y*-component of the external electric field is shielded and ionization inside the cathode layer decreases. Another feature is the behaviour of the current on the plateau of the electrical pulse. This stage with a slowly decreasing electrical current (3–15 ns in figure 7) is due to the formation of the near-surface plasma layer [22], and is observed in both the calculations and measurements. The current in both calculations and experiments, and in both polarities, decay progressively to 0 at almost the same rate in the tail.

The formation of the near-surface plasma layer is an issue which is extremely complicated for experimental study. In the available numerical calculations [12, 19, 22, 24], the electric field in the case of the negative polarity discharge has a diffuse structure. Although some authors [19] say that 'there are no streamers at negative polarity', we would prefer to maintain, similar to [24], the terms 'negative streamers' and 'positive streamers'. In both negative and positive streamers, there is a sheath region near the dielectric. In the sheath, the strong electric field is directed perpendicular to the dielectric surface, and the electron density is low. The thickness of the sheath predicted numerically for atmospheric pressure SDBDs is a few microns for the negative polarity discharge and 40–50 μm for the positive polarity discharge. Later in the paper, we will turn our attention to the role of the sheath for (i) streamer propagation; (ii) production of active species; (iii) resulting hydrodynamic perturbations.

5.2. Modeling of electron density and electric field

Two approaches to the nSDBD description—theoretical and experimental—are different, first of all, by the definition of 'streamer'. In the theory and numerical calculations, a streamer is represented by isolines of the electron density and/or the electric field. In the experiments, measurements of the electron density are complicated because of relatively low absolute values of n_e and high demands to spatial resolution. Two wavelength Shack–Hartmann-type laser wavefront sensors were successfully used to measure the 2D time-resolved electron density in extinguishing atmospheric arc discharges with currents of several tens of amperes [50], but the lower electron densities reported in [50] were on the order of 10^{17} cm^{-3}. Measurements of the electric field are limited by measurements of the ratio of emission of two bands with different thresholds integrated over the thickness of the streamer [11, 12], as discussed above. A picosecond four-wave mixing can be adapted for the measurements of the electric field in a surface discharge, but at present only the measurements in volumetric nSDBD are available [15]. As a result, in the experiments, the surface streamer is defined as a region corresponding to the optical emission in the UV and visible range of spectra. The aim of the next two sections is to provide a comparison between the two ways of describing a surface streamer.

The evolution of the electron density in the negative and positive streamer at four successive time moments is shown in figure 8. The time moments are different: 1, 5, 10 and 15 ns for negative polarity and 2, 4, 6 and 8 ns for positive polarity. The point (0, 0) corresponds to the triple point. The scale on the *X*-axis is also different: 0–10 mm for negative polarity, and 0–20 mm for positive polarity. The vertical scale is the same for negative and positive polarity; a represented region takes 1.1 mm above the dielectric electrode. Similar to [22, 24], a negative polarity streamer is more diffuse; this can be seen from the 2D plots of the electron density near the high voltage electrode. For both polarities, the electron density increases and then decreases when moving in a vertical direction from the dielectric surface. For positive polarity, the thickness of the region of a high electron density is approximately two times higher.

With time, a diffuse 'cloud' of the electron density near the high-voltage electrode at negative polarity remains virtually unchanged with a typical vertical size of about 0.4 mm, in excellent correlation with the calculations of [24]. The size of the streamer head is much smaller than the size of the 'cloud'—about 60 μm at 5 ns at a distance of 7.5 mm from the high-voltage electrode, and about 30 μm at a distance of 10 ns at 9.6 mm from the high-voltage electrode. The cross-section of the negative streamer maintains a triangle-like shape with a diffuse 'cloud' near the high-voltage electrode

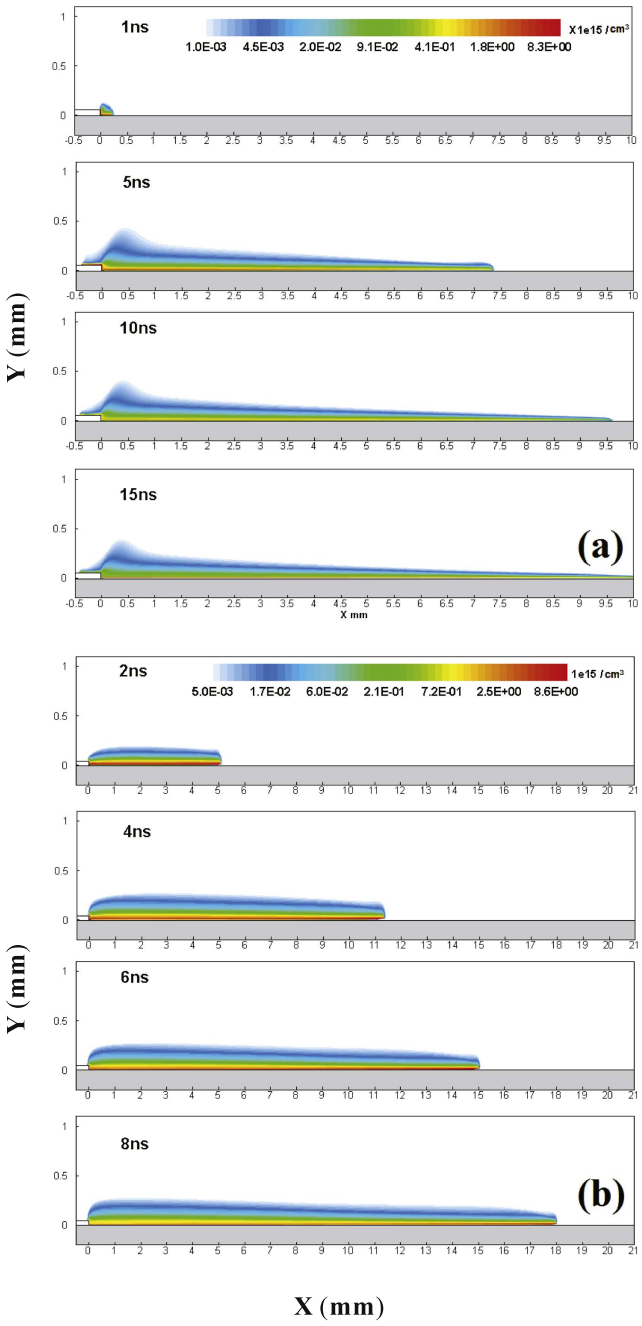

Figure 8. The evolution of the electron density for negative (a) and positive (b) streamers. Time instants are 1, 5, 10, 15 ns for the negative polarity streamer and 2, 4, 6 and 8 ns for the positive polarity streamer. The scale on the *OX*-axis is 0–10 mm for the negative polarity streamer and 0–20 mm for the positive polarity streamer. The scale on the *OY*-axis and the scale for the electron density are the same for both polarities.

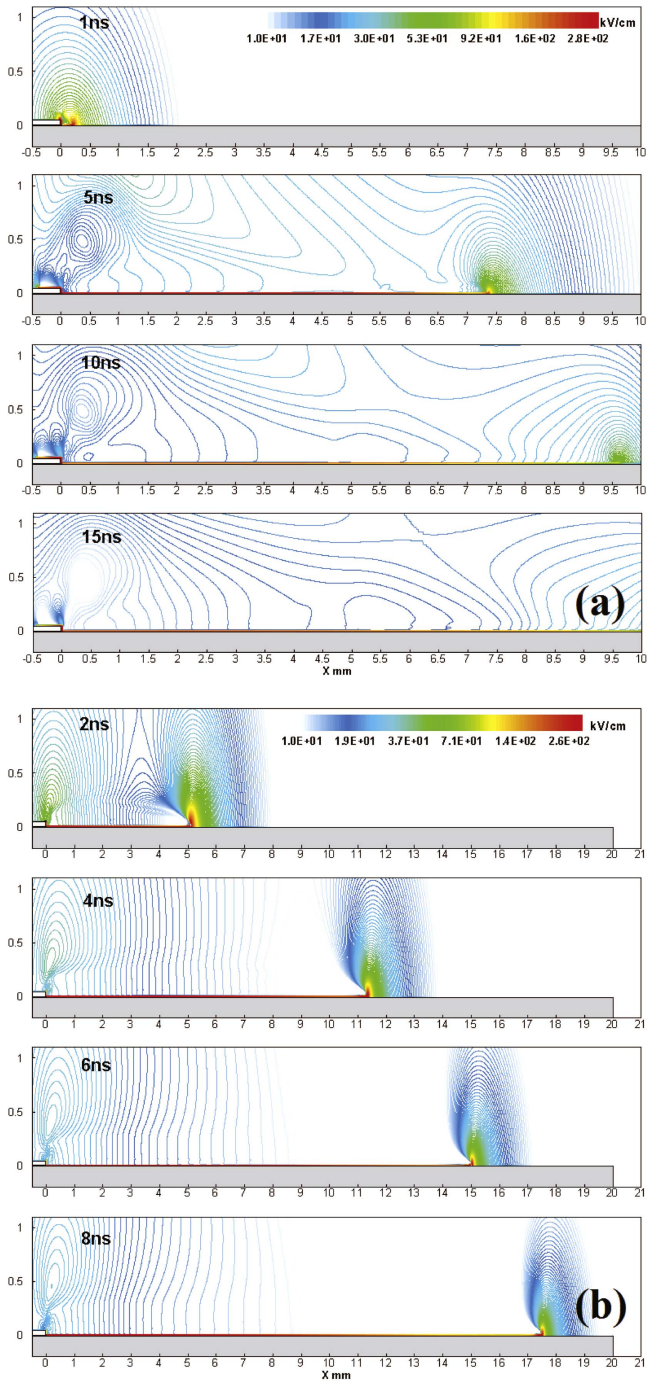

Figure 9. The evolution of the absolute value of the electric field for negative (a) and positive (b) streamers. Time instants are 1, 5, 10, 15 ns for the negative polarity streamer and 2, 4, 6 and 8 ns for the positive polarity streamer. The scale on the *OX*-axis is 0–10 mm for the negative polarity streamer and 0–20 mm for the positive polarity streamer. The scale on the *OY*-axis and the scale for the electric field are the same for both polarities.

and a 'needle-like' head during the discharge propagation along the surface. For positive polarity, a 'sandwich-like' structure is observed for the electron density: the thickness of the layers with a constant electron density changes only slightly along the streamer.

To compare the behavior of the emission of a particular molecular band for different polarities, information regarding the electron density and the electric field is required. The evolution of the absolute value of the electric field in the negative and positive streamers at the same time instants of the electron density is shown in figure 9. For both polarities, high values of the electric field are observed in the streamer head. The maximum of the color scale presented by figure 9 corresponds to approximatively 300 kV cm^{-1} (1200 Td at

atmospheric pressure), in reasonable correlation with [12, 24]. Higher electric fields in the head of a positive polarity streamer at a distance of a few cm from the high-voltage electrode compared to negative polarity are also in correlation with the calculation of [24].

A principal difference in the behavior of the electric field for negative and positive polarity is that at negative polarity, a weak electric field is observed at significant distances from the dielectric in the vertical direction, starting from tens of microns to $y = 1$ mm and more. The absolute value, $(E/N)^* \leqslant$ 20–30 kV cm^{-1}, or 80–120 Td (light blue color in figure 9), is not enough for efficient ionization, so it is often neglected in a 'standard' streamer representation, where the electron density and the ionization source are typically plotted. But these values are efficient for the excitation of the $N_2(C^3\Pi_u)$-state of molecular nitrogen. Indeed, in the outer perimeter of the streamer head, the electric field is $(E/N) \approx$ 50–100 kV cm^{-1}, or 200–400 Td (green color in figure 9). The ratio of the rates of excitation of the $N_2(C^3\Pi_u)$-state by electron impact and of ionization at $E/N = 400$ Td is about 3, while at $E/N = 80$ Td, this ratio is equal to 240. As a result, the emission of the second positive system should be visible, not only in the front and near the electrode, but also between them. At positive polarity, the field between the streamer head and the near-electrode region at significant distances, $y \geqslant$ 30–50 μm, is low, $E/N \ll (E/N)^*$. As a result, the calculated emission of the second positive system of N_2 in the case of positive polarity should be visibly concentrated in the streamer head and near the high-voltage electrode.

The aim of the next section is to compare, for both polarities, the calculated and measured experimental 2D time-resolved streamer emission for the second positive system of molecular nitrogen, and to compare the numerical and experimental streamer 'appearance' for the same conditions.

5.3. Modeling and measurements of 2D time-resolved streamer emission

The emission observed by 2D imaging is mainly (at least with the accuracy of a few percent) the emission of the second positive system of molecular nitrogen. The only 'concurrent' of the second positive system in the UV and visible (200–800 nm) range of spectra at short time periods at high electric fields in air is the first negative system of N_2, with a strong $v' = 0 \rightarrow v'' = 0$ band at $\lambda = 391.4$ nm, partly overlapped with $3 \rightarrow 6$, $\lambda = 389.5$ nm and $2 \rightarrow 5$, $\lambda = 394.3$ nm bands of the second positive system. We performed a set of additional experiments with 340 ± 5 nm and 390 ± 5 nm narrow band filters, trying to separate the emission from the second positive and the first negative system at the front of the discharge with a time resolution of 0.5 ns, and we failed; no one time instant and no spatial zone, where the emission of $\lambda = 391.4$ nm can be clearly distinguished on the background of the 2^+ system under the mentioned method of visualization, were found. Two conclusions were made from these preliminary experiments: (i) using photomultiplier tubes with a gain an order of magnitude higher than the ICCD camera gate and selecting the emission strictly by molecular bands, it is possible to separate experimentally the first positive and second negative systems in the nSDBD [12] and to judge the absolute values of the electric field [13, 14]. The experiments to separate the emission in 2D in the time-resolved mode are possible but demand more precautions. (ii) The emission observed experimentally and presented below is the emission of the second positive system of molecular nitrogen.

The emission intensity at any point in any time instant is defined by a product of electron density n_e and the rate constant of N_2 excitation by electron impact, which is a function of the reduced electric field E/N. The density of $N_2(C^3\Pi_u)$ in nSDBD is governed by the following equation:

$$\frac{d[N_2(C^3\Pi_u)]}{dt} = k_e(E/N)n_e[N_2] - \frac{[N_2(C^3\Pi_u)]}{\tau_0} - \sum_i k_q^i[N_2(C^3\Pi_u)][M_i], \quad (14)$$

where $k_e(E/N)$ is a rate constant of excitation of $N_2(C^3\Pi_u)$ by electron impact, τ_0 is the lifetime, k_q^i and $[M_i]$ are the rate constants of quenching and the densities of quenchers respectively, and the emission intensity is proportional to the density of molecules on the upper state: $I \sim [N_2(C^3\Pi_u)]$.

The calculated 2D map of $N_2(C^3\Pi_u)$ emission at seven successive time moments is shown in figure 10. The time moments are different: 1, 2, 3, 4, 5, 10 and 15 ns for negative polarity and 1, 2, 3, 4, 5, 6 and 8 ns for positive polarity. The scale on the *OX*-axis is 0–10 mm for negative polarity, and 0–20 mm for positive polarity, similar to figures 8 and 9. The vertical scale is the same for negative and positive polarity and twice smaller than for the electron density and electric field; a represented region takes 0.6 mm above the dielectric layer.

At negative polarity, two distinctive features of the calculated profile of emission should be mentioned (figure 10(a)): (i) during the first few nanoseconds, the emission reproduces the behavior of the electron density; (ii) after 10 ns, the emission flattens against the dielectric, and the visible thickness of the discharge decreases by a factor of 4–8. The observed gradual flattening of the emission is connected with a slow decrease of the absolute value of the electric field in the 'body' of the streamer channel, tens and hundreds of micrometers above the dielectric surface.

The evolution of the positive polarity nSDBD (figure 10(b)) also reflects the distribution of the electric field in time and space. Two regions of the high electric field and relatively high electron density are observed—in the streamer head and near the high voltage electrode. As a result, the emission pattern is divided into two parts (2–4 ns), more and more separated in space with time, and finally (6–8 ns and more) no optical emission is observed from the streamer 'body' between the streamer head and near-electrode region.

The calculated emission presented in figure 10 was compared with the measured emission plotted in figure 11. The experimental 2D map of the emission is taken at 0.5, 1, 1.5, 2, 2.5, 8 and 10 ns for both polarities. A synchronization between the calculated and measured picture is present but the initial moment can be shifted by 0.5–1.5 ns; in the

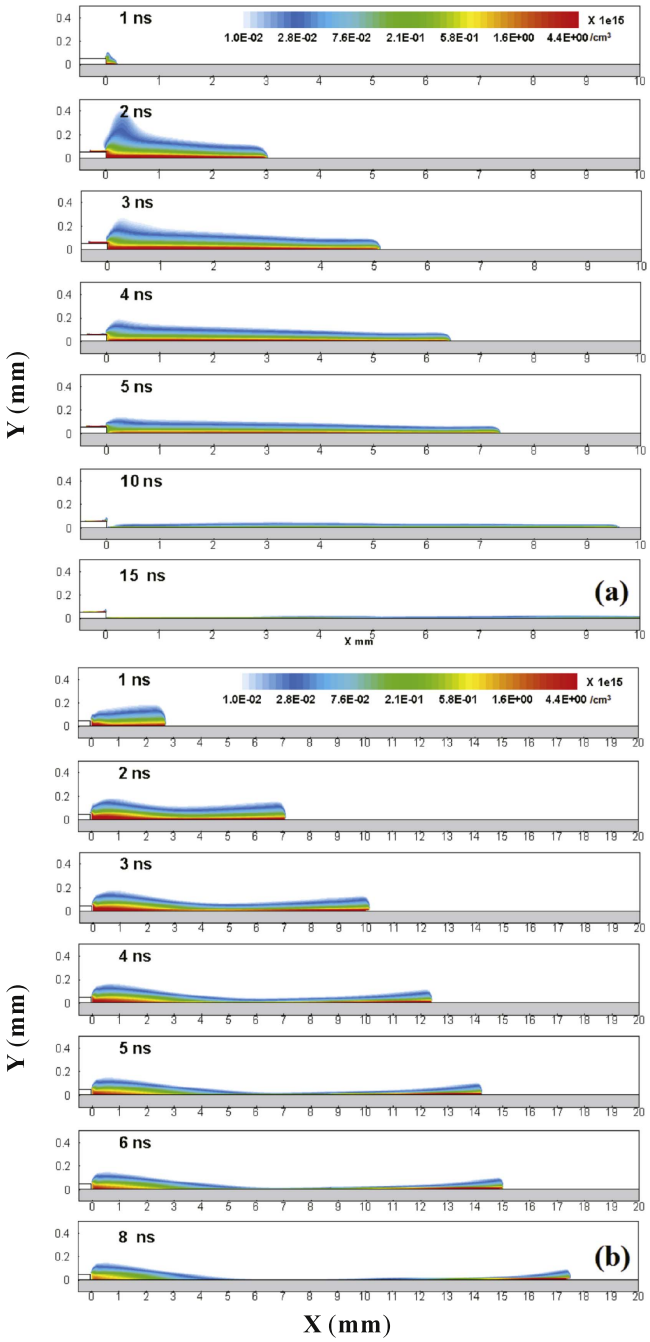

Figure 10. The evolution of the calculated $N_2(C^3\Pi_u)$ density in unit $\times 10^{15}/cm^3$ for negative (a) and positive (b) streamers. Time instants are 1, 2, 3, 4, 5, 10, 15 ns for the negative polarity streamer and 1, 2, 3, 4, 5, 6 and 8 ns for the positive polarity streamer. The scale on the *OX*-axis is 0–10 mm for the negative polarity streamer and 0–20 mm for the positive polarity streamer. The scale on the *OY*-axis and the scale for the $N_2(C^3\Pi_u)$ density are the same for both polarities.

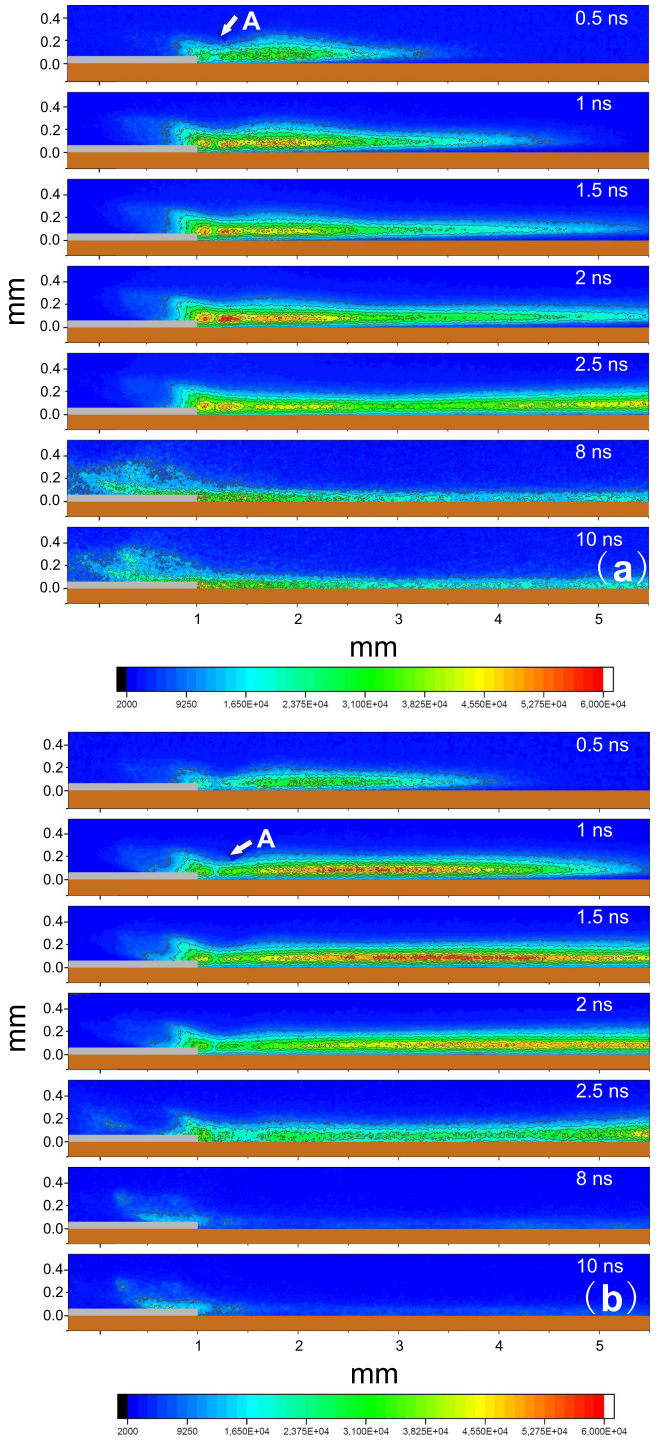

Figure 11. The evolution of the measured $N_2(C^3\Pi_u) \rightarrow N_2(B^3\Pi_g)$ emission intensity (a.u.) for negative (a) and positive (b) streamers. The span of the electrode system is $W = 25$ mm. The ICCD camera gate is equal to 0.5 ns. Time delays relative to the start of the discharge are 0.5, 1, 1.5, 2, 2.5, 8, 10 ns for both polarities. The scales on the *OX* and *OY*-axes and the sensitivity of the ICCD camera are the same for both polarities. See the text for the explanation of point A.

experiments, the $t = 0$ instant was defined as a point 0.5 ns before the first image with a visible emission. No special experiments were conducted to synchronize the electrical and optical measurements or to measure the emission at the beginning of the discharge with increased ICCD sensitivity. No reverse Abel procedure has been conducted, but a qualitative analysis of the profile of emission assuming that all streamers are identical shows that the maximum of emission is observed inside the streamer channel, decreasing to the periphery. The picture is not symmetrical; the central 'axis' of emission is shifted toward the dielectric. The maximum of emission is observed at a distance of about 35% of the

diameter of the total emission channel over the dielectric. It should be noted that the emission intensity near the surface was not corrected for the solid angle; as the angle of the light collection decreases when approaching the dielectric, a visible intensity of emission should also decay.

For negative polarity, the shape of the measured emission profile during the first few nanoseconds is similar to the shape of the calculated emission and electron density. Similar to the electron density, a vertical cross-section of the negative streamer has a triangle-like shape with a diffuse 'cloud' near the high-voltage electrode and a 'needle-like' head during the discharge propagation along the surface. After 8–10 ns, similar to that observed in the calculations, the optical emission flattens and significantly decreases in amplitude.

For the positive polarity discharge, the velocity of propagation is much higher starting from the first nanoseconds. At the time period 8–10 ns and later, no emission is observed behind the front of the streamer. A 'separation' of the two regions with a decrease in the thickness of the streamer in the central part can be clearly seen at 2.5 ns in figure 11.

A feature which does not exist in the numerical modeling is a 'bottleneck' separating a bright near-electrode region 150–200 μm in length and the main streamer channel. The bright region exists from the very beginning of the streamer propagation; it elongates and disappears at 2–2.5 ns. The feature is experimentally observed for both polarities of the high-voltage pulse (see point A in figure 11).

It is important to note that the thickness of the region of a well-pronounced $N_2(C^3\Pi_u)$ emission ('the emission zone') is about 200–250 μm, well above the calculated thickness of the near-dielectric region of high electric fields, a few micrometers for negative polarity and tens of micrometers for positive polarity. When the threshold of excitation of the $N_2(C^3\Pi_u)$-level is 11.03 eV [51], the emission describes a region where the electric field is still high $(E/N)^* \sim 80$–100 Td, and the electron density is already high enough to provide the efficient excitation of electron levels, and so, efficient dissociation. The emission zone is the most important zone of the discharge when considering the nSDBD as a plasma-chemical reactor.

Another important issue is the temperature increase due to fast gas heating [28] on tens–hundreds of nanoseconds and more due to VT-relaxation [52] on a microsecond time scale. A local increase of gas temperature can (i) provoke a chemical reaction when the reaction rate is an Arrhenius exponential function of gas temperature; (ii) create a hydrodynamic perturbation and a low density region. The last action is accepted to be the most important factor in gas flow control using nSDBDs [53].

5.4. Hydrodynamic perturbations initiated by nSDBD

Hydrodynamic response was calculated using the same mesh as for plasma equations. Unlike widely used mesh mapping or interpolating methods in coupling fluid and plasma code, using the same mesh for both plasma and fluid sacrifices the resolution of the fluid problem far away from the electrode, but enables the possibility of resolving the early response of the fluid during and after the discharge in a very short time and very fine spatial scale.

The generation and propagation of compression waves in nanosecond SDBDs is one of the most typical nSDBD phenomena observed both in experiments and simulations [4, 42, 54, 55]. In the present paper, the calculation is focused mainly on the formation and propagation of the hydrodynamic perturbation within a small spatial scale at an early stage, $t < 1$ μs, referred to as the 'early stage'. The longer time scale, $1 < t < 5$ μs is considered mainly for the reference to the majority of available experiments.

Figure 12 shows the calculated pressure map after the discharge initiated by positive and negative polarity voltage pulses. In both cases, a strong perturbation of pressure is observed along the dielectric surface ('wave 1' hereinafter) and at the edge of the exposed electrode due to fast and local heat release in chemical reactions ('wave 2'). The waves propagate with approximately constant slightly supersonic velocity at $t < 2 - 2.5$ μs and then slow down. For negative polarity discharge, waves 1 and 2 are well distinguished and propagate with $v_1 = 1.2\,M$ and $v_1 = 1.5\,M$ respectively. For positive polarity nSDBD, wave 1 is more uniformly distributed above the dielectric; $v_1 = v_2 \approx 1.35\,M$. For negative polarity, an increased energy release in the near-cathode region can be clearly seen ('wave 3', $v_3 = 1.5\,M$). The near-cathode layer with elevated specific energy deposition and an increased density of dissociated oxygen has been observed in the calculations for atmospheric pressure air performed in [56]. A typical size of the layer was about 10 μm in the x–direction at 30 ns from the moment the discharge began. The authors of [56] concluded that the discharge of negative polarity should ignite the combustible mixtures better due to a concentrated energy release, and they proved this experimentally on the example of C_2H_2:air mixtures for initial ambient temperatures and initial pressures in the range of 0.6–1 atm. A typical shadowgraph and Schlieren measurements reported for a few microseconds and longer do not demonstrate a significant difference for different polarities of the discharge [57]. To the best of our knowledge, no direct experimental confirmation of a high energy release at the early stage was available before in the literature.

The shadowgraph images of the nSDBD discharge in the same configuration as the experimental system described in the above optical emission images (figure 11) are presented in figure 13. Already at 200 ns, a perturbation, which began from the near-dielectric zone along the streamer channel (wave 1), is clearly seen for both polarities. The perturbation moves up in the vertical direction. At this stage, the perturbation near the high-voltage electrode (mainly above the electrode) can be distinguished only for negative polarity (wave 3). At a later time scale, $t > 1$ μs, experimental measurements provide fairly similar impressions for negative and positive polarity: a cylindrical wave propagating from the edge of the high-voltage electrode (wave 2) and a set of waves, 'enveloping' each streamer (wave 1). A qualitative difference between the experiments and numerical modeling is an appearance of these waves. In the numerical modeling, waves 1 and 2 appear simultaneously; the intensity of wave 2

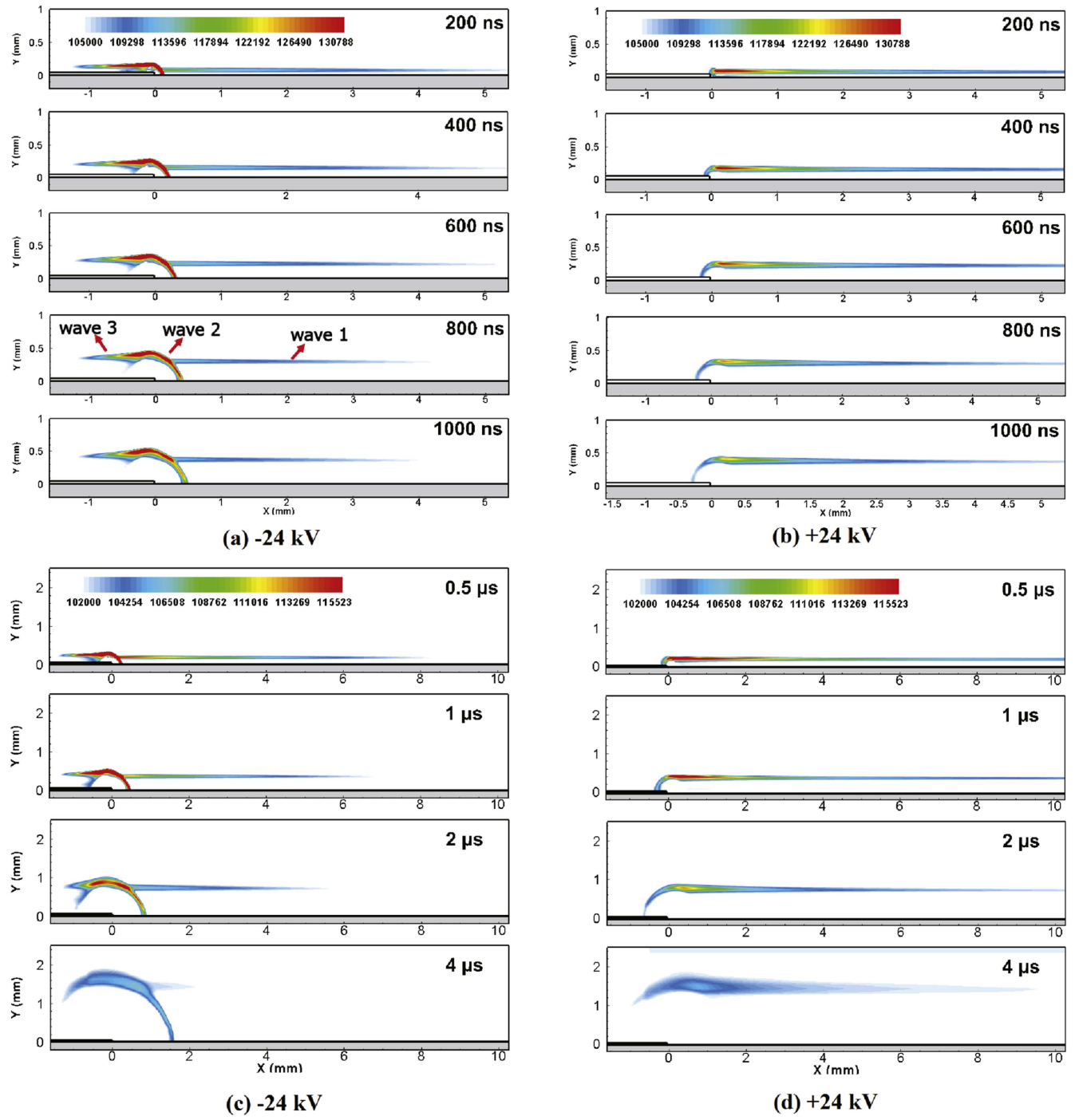

Figure 12. The evolution of the calculated pressure perturbations (in Pa) (a), (b) short time scale, 0.2–1 μs, (c), (d) long time scale, 0.5–4 μs; (a), (c) negative polarity discharge, (b), (d) positive polarity discharge. The *OX* and *OY* scales are kept similar for (a), (b) cases and similar for (c), (d) cases. The short-time scale maps are zoomed relative to the long-time scale images. Waves 1, 2 and 3 are marked in 800 ns frame (see the explanation in the text).

at negative polarity is stronger, and at positive polarity is comparable to the intensity of wave 1. In the experiments, wave 1 along the streamers appears first. Wave 2, from the edge of the electrode, becomes clearly visible only starting from 1 μs. The intensity of wave 1 enveloping the streamers is visibly higher at the early stage. The intensities of waves 1 and 2 are nearly equal at $t > 1$ μs. The additional perturbation above the high-voltage electrode, wave 3, observed in the numerical modeling and in the experiments at negative polarity, appears at an early stage and is visible up to a few microseconds in the modeling, but does not exist a few microseconds into the experiment.

Comparing the numerical modeling and experiments, it is important to note that in fast gas heating, different classes of reactions can be selected as a function of the reduced electric field. At high electric fields, $E/N > 500$ Td, the main heat

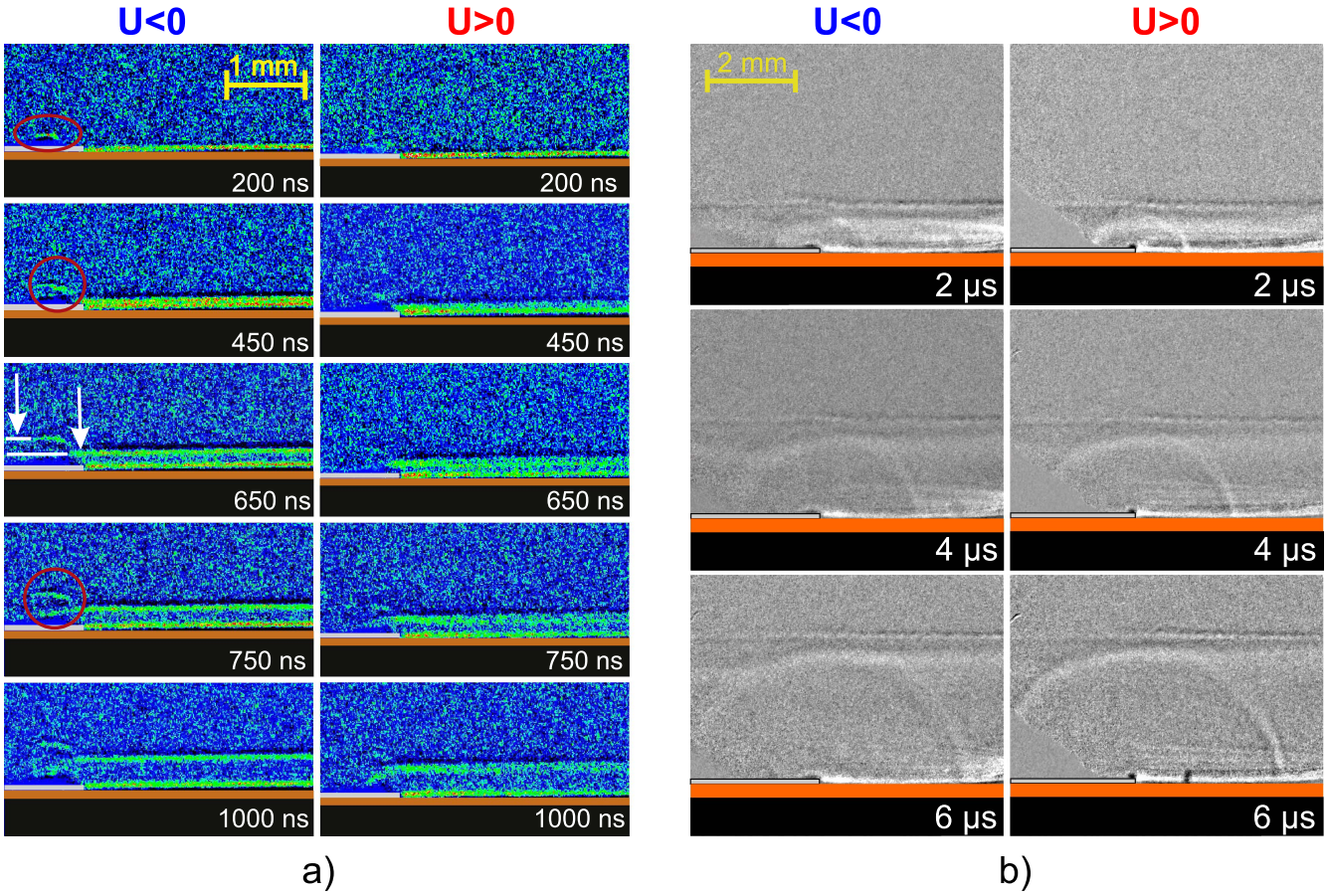

Figure 13. Hydrodynamic perturbations observed experimentally by the shadowgraph technique for different polarities of the high-voltage pulse (a) short time scale, 0.2–1 μs; (b) long time scale, 2–6 μs.

release is due to the reactions involving charged particles, while for $E/N \approx$ 200–400 Td, quenching of $N_2(C^3\Pi_u)$ and $N_2(B^3\Pi_g)$ states by molecular oxygen provide more than 50% of the fast gas heating [28]. At our experimental conditions, the main picture of the hydrodynamic perturbations is formed due to the reactions of the quenching of $N_2(C^3\Pi_u)$ and $N_2(B^3\Pi_g)$ by molecular oxygen, and the reaction of $O(^1D)$ quenching by O_2. Calculations show that a different appearance of wave 3 and waves 1 and 2 correlates with the quenching of the $N_2(C^3\Pi_u)$ level: at negative polarity, $N_2(C^3\Pi_u)$ is produced in the thin layer over the high-voltage electrode; as a result, the flat wave 3 (see figure 13(a)) starts from the electrode. In the authors' opinion, the sensitivity of the hydrodynamic perturbation to kinetics can be used in the future to 'measure' the input of different classes of reactions in fast gas heating, comparing experimentally and numerically a fine structure of hydrodynamic perturbations at the early time scale, $t < 1$ μs.

5.5. Parametric calculations: different dielectric permittivities and different thicknesses of the dielectric layer

To analyze nSDBD morphology and velocity at different conditions, a parametric study has been performed. Calculations were performed for atmospheric pressure air and for the parameters of the high-voltage pulses of the present work for two different cases. The case (A) was calculated for a constant thickness of the dielectric, $d = 0.5$ mm, and for three different dielectric permittivities: $\varepsilon_1 = 4$, $\varepsilon_2 = 16$ and $\varepsilon_3 = 80$. The case (B) considered the constant dielectric permittivity, $\varepsilon = 4$, and the thickness of the dielectric changed: $d_1 = 0.5$ mm, $d_2 = 1$ mm and $d_3 = 5$ mm.

Figure 14 presents the instantaneous speed of the discharge propagation front for different ε values and a few selected 2D maps of the electron density and electric field for different polarities of the high-voltage pulse. The ascending branch of the velocity in the early stage of the discharge development has been never observed experimentally. According to the calculations, the $N_2(C^3\Pi_u)$ emission intensity at $t < 1$ ns is 1–2 orders of magnitude lower than for the longer time periods. This is the reason why only the descending branch of the velocity dependence upon distance is compared with the experimental data in figure 6(b). A change in the discharge velocity and morphology is directly related to changes in the deposition of the electrical charge and changes of the electric field in the vicinity of the dielectric.

At negative polarity, the picture is complex. Already in the baseline case (see figure 8(a)) the electron density pattern can be considered as a combination of two distinctive shapes: a diffuse 'cloud' near the high-voltage electrode, and a triangle-like narrow pattern, sliding along the surface of the dielectric. With an increase in ε, the 'cloud' elongates, propagating with a relatively slow speed. A triangle-like pattern

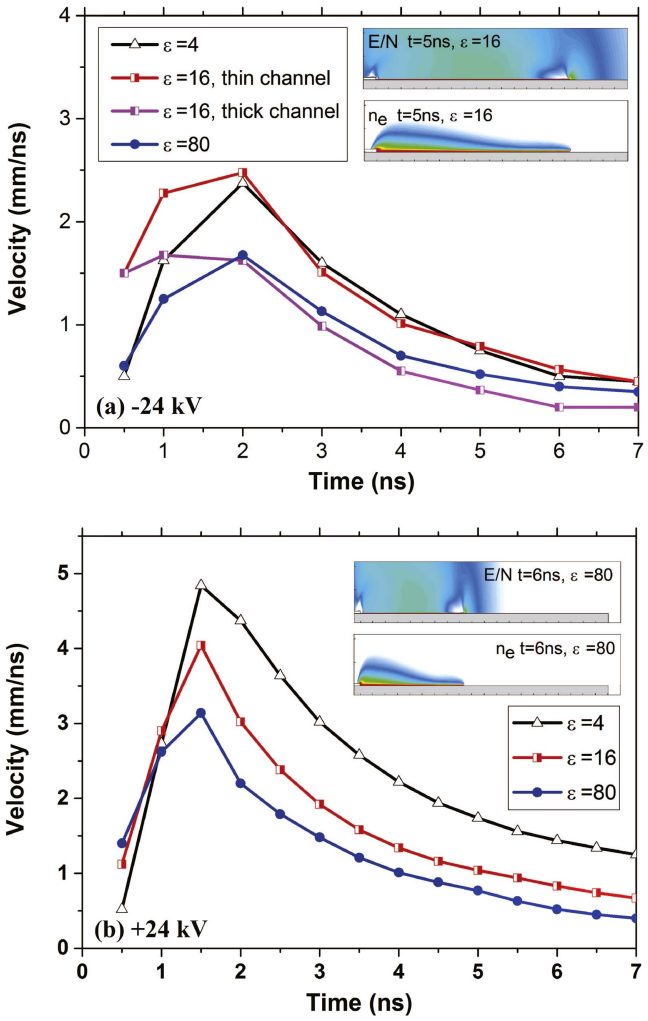

Figure 14. Parametric calculations for different dielectric permittivities ε, velocity of the discharge front as a function of time for (a) negative and (b) positive polarity of the high-voltage pulse. Designations 'thin channel' and 'thick channel' at $\varepsilon = 16$ correspond to the 'needle-like' and 'cloud-like' parts of the channel of the negative polarity streamer described in the text. The inserts in the upper right corner of the figures show 2D maps of the electric field and electron density at $t = 5$ ns and $\varepsilon = 16$ for (a) and at $t = 6$ ns and $\varepsilon = 80$ for (b).

propagates faster but starting from a given distance, the field behind the streamer head decreases noticeably. With a further increase of ε in the calculations, the needle-like pattern disappears, the discharge structure changes, and only a cloud-like structure propagates along the dielectric—the electric field and electron density being enough for the $N_2(C^3\Pi_u)$ measurements. The 'cloud-like' structure and the triangle-like pattern are designated in figure 14(a) as a 'thick channel' and 'thin channel' respectively; the difference in the velocities can be clearly seen.

For positive polarity discharge, with an increase in ε, the electric field map stays similar to the baseline case ($d = 0.5$ mm, $\varepsilon = 4$) with the only difference being that the field in the streamer channel increases with ε. As a result, (i) the thickness of the electron density pattern increases (0.5 mm at $\varepsilon_3 = 80$ instead of 0.1 mm at $\varepsilon_1 = 4$) transforming to a shape close to n_e at negative polarity, and (ii) a combination of high electric fields in the streamer channel and high electron density results in high densities of $N_2(C^3\Pi_u)$. With an increase in the dielectric permittivity, a channel of the positive polarity streamer should become 'visible' experimentally.

For both polarities, the electric current increases with ε, reaching 50–100 A cm^{-1} for $\varepsilon_2 = 16$ and 150–200 A for $\varepsilon_3 = 80$. The following conclusion can be made from the numerical calculations: with an increase in ε, the streamer thickness (calculated by electron density) increases significantly, by a factor of 5 as ε changes from 4–80; the electric fields, for $\varepsilon > 10$, should be enough to observe the emission from the streamer channel at both polarities of the high-voltage pulse. Special care should be taken to avoid a breakdown of the dielectric with increasing electrical current.

Calculations for different thicknesses of the dielectric show the following: for negative polarity discharge, the 'cloud-like' feature will stay near the high-voltage electrode, and the 'needle-like' shape of the electron density will transform to a shape close to the streamer at positive polarity but with lower values of the electron density. The electric field behind the streamer head will drop down, and finally, the emission from the streamer channel will not be detected experimentally. For positive polarity discharge, with a dielectric thickness increase, the electric field in the channel will be totally concentrated in the narrow, tens of microns gap near the dielectric, and the electron density layer will not change noticeably. As a consequence, no emission will be seen experimentally from the streamer channel. The electrical current decreases noticeably to 12–25 A cm^{-1} at $d_2 = 1$ mm and to 3–6 A cm^{-1} at $d_3 = 5$ mm.

Thus, it can be concluded that varying the dielectric properties of the electrode is a more promising way to obtain a comparison between the theoretical predictions and experimental observations.

6. Conclusions

A 2D parallel PASSKEy code coupling plasma and hydrodynamics has been developed to model the development of an nSDBD. The computational model is a 2D self-consistent description of a multi-species mixture under the action of discharge and hydrodynamic expansion in the early afterglow, with detailed chemical kinetics and energy release in chemical reactions. The code is optimized using a hybrid OpenMP–MPI parallel approach. The kinetic scheme considers 13 species and 38 reactions, including reactions responsible for fast gas heating in N_2:O_2 mixtures. The code is validated using benchmarks for volumetric and surface streamers available in the literature .

Calculations of negative and positive polarity streamers have been performed for atmospheric pressure air, voltage amplitude $U = \pm 24$ kV on the electrode, dielectric thickness $d = 0.5$ mm and dielectric permittivity $\varepsilon = 4$. The results were compared with experimentally obtained data. The discharge velocity, electrical current, time-resolved structure of 2D emission of the second positive system of molecular

nitrogen and hydrodynamic perturbation measured in the time interval 0.2–5 μs were the subject of comparison. To our knowledge, this is the first detailed comparison of numerical calculations and experiments performed for the same parameters of nSDBD. In addition, parametric calculations for $d = 0.5$–5 mm and $\varepsilon = 4$–80 have been performed for both polarities.

It was confirmed that for different geometries of electrodes, the velocity of the discharge front is about 2–3 mm ns^{-1} for negative and ~5 mm ns^{-1} for positive discharge at the early stage of propagation. It drops down to 0.1 mm ns^{-1} and less for the negative polarity streamer, while the positive polarity streamer continues to propagate with a velocity progressively decreasing to 0.4–0.5 mm ns^{-1} at the end of the pulse. A good correlation between the experimental data and numerical calculations confirm that the model takes into account the main processes responsible for surface streamer propagation. The measured and calculated electrical current through the discharge are in reasonable correlation, comprising 20–50 A cm^{-1} depending upon the conditions.

2D maps of the electron density, the absolute value of the electric field and $N_2(C^3\Pi_u)$ density were calculated. The existence of narrow zones of a high electric field, a few microns for negative polarity discharge and a few tens of microns for positive polarity discharge, has been confirmed numerically. The 2D maps of the emission intensity for two polarities of the nSDBD in the plane perpendicular to the electrode system were obtained experimentally for the first time. The main aim of the calculations was to compare the structure of the experimentally measured and calculated $N_2(C^3\Pi_u)$ distribution, and to analyze the emission of the second positive system of molecular nitrogen on the basis of 2D distributions of the electron density and electric field.

Electron density distribution at negative polarity consists of two distinctive zones: a 'cloud-like' diffuse zone near the high-voltage electrode, and a 'needle-like' zone propagating along the dielectric. The positive polarity streamer produces a relatively uniform constant thickness pattern of the electron density along the dielectric. The electric field in the bulk of the streamer channel of negative polarity is high—about 100 Td; for the streamer channel of positive polarity, the field is low—less than 40 Td. The calculated $N_2(C^3\Pi_u)$ density repeats the main peculiarities of the distributions of electrons and field in time and space. The thickness of the channel of the surface streamer calculated from the distribution of the $N_2(C^3\Pi_u)$ density is about 1.5 times larger than the radius calculated from the electron density in the first 5 ns and then becomes thinner. The most distinctive experimentally observed difference, namely a non-zero level of emission in the developed channel in the negative polarity streamer and absence of emission in the positive polarity streamer, is reproduced in the calculations.

Weak shock waves, appearing around the streamers and near the edge of the high-voltage electrode at sub-microsecond time scale, are a consequence of fast gas heating in plasmachemical reactions. The main processes responsible for the formation of hydrodynamic perturbation are reactions of the quenching of $N_2(C^3\Pi_u)$ and $N_2(B^3\Pi_g)$ by molecular oxygen, and the reaction of $O(^1D)$ quenching by O_2. A specific zone of energy release corresponding to $N_2(C^3\Pi_u)$ production, was found numerically and experimentally over the high-voltage electrode for the discharge of the negative polarity.

Parametric calculations provided for three different dielectric permittivities ($\varepsilon_1 = 4$, $\varepsilon_2 = 16$ and $\varepsilon_3 = 80$ and three different values of the thickness of the dielectric ($d_1 = 0.5$ mm, $d_2 = 1$ mm and $d_3 = 5$ mm) show that discharge changes in quite a complex way. In general, the discharge slows down with ε and d, but changes in the discharge morphology cause a non-monotone behavior of the discharge velocity in the negative polarity discharge with an increase in ε. The electrical current and electron density increase with ε and decrease with d. The optical thickness of the streamer significantly increases with ε and slightly increases with d.

For all the calculated cases, there exists a long region of plasma with relatively uniform parameters, a channel, where plasma properties, in spite of the non-uniformity of the surface streamer in the direction perpendicular to the dielectric, can be analyzed on the basis of the electrical current and $N_2(C^3\Pi_u)$ emission. This region is the most important when analyzing nSDBD as a source of active species.

Acknowledgments

The work was partially supported by the French National Agency, ANR (ASPEN Project, ANR-16-CE30-0004-01), by LabEx Plas@Par, as part of the 'Investments for the Future' French National Program ANR–11–IDEX–0004–02, and by Linked International Laboratory LIA KaPPA (France—Russia). The authors are grateful to Dr Nikolay Popov (MSU) and Dr Anne Bourdon (LPP) for numerous discussions concerning the kinetics of fast gas heating and photoionization.

ORCID iDs

Yifei Zhu https://orcid.org/0000-0001-8989-0051

References

[1] Leonov S B, Adamovich I V and Soloviev V R 2016 Dynamics of near-surface electric discharges and mechanisms of their interaction with the airflow *Plasma Sources Sci. Technol.* **25** 063001

[2] Borisov V M, Davidovskiĭ A M and Borisovich O 1982 Experimental investigation of the characteristics of a planar surface discharge *Quantum Electron.* **12** 1403–8

[3] Opaits D, Roupassov D, Starikovskaia S, Starikovskii A Y, Zavialov I and Saddoughi S 2005 Plasma control of boundary layer using low-temperature non-equilibrium plasma of gas discharge *43rd AIAA Aerospace Sciences Meeting and Exhibit* 1180, 2005

[4] Starikovskii A Y, Nikipelov A, Nudnova M and Roupassov D 2009 SDBD plasma actuator with nanosecond pulse-periodic discharge *Plasma Sources Sci. Technol.* **18** 034015

[5] Leonov S, Opaits D, Miles R and Soloviev V 2010 Time-resolved measurements of plasma-induced momentum in air and nitrogen under dielectric barrier discharge actuation *Phys. Plasmas* **17** 113505

[6] Rethmel C, Little J, Takashima K, Sinha A, Adamovich I and Samimy M 2011 Flow separation control using nanosecond pulse driven DBD plasma actuators *Int. J. Flow Control* **3** 4

[7] Bisek N J, Poggie J, Nishihara M and Adamovich I 2014 Hypersonic flow over a cylinder with a nanosecond pulse electrical discharge *J. Thermophys. Heat Transfer* **28** 18–26

[8] Bayoda K, Benard N and Moreau E 2015 Nanosecond pulsed sliding dielectric barrier discharge plasma actuator for airflow control: electrical, optical, and mechanical characteristics *J. Appl. Phys.* **118** 063301

[9] Sokolova M, Kozlov K, Krivov S, Samoilovich V and Tatarenko P 2009 Studying emission from a surface discharge in dry air *Tech. Phys. Lett.* **35** 207–10

[10] Hoder T, Brandenburg R, Basner R, Weltmann K, Kozlov K and Wagner H 2010 A comparative study of three different types of barrier discharges in air at atmospheric pressure by cross-correlation spectroscopy *J. Phys. D: Appl. Phys.* **43** 124009

[11] Nudnova M, Aleksandrov N and Starikovskii A Y 2010 Influence of the voltage polarity on the properties of a nanosecond surface barrier discharge in atmospheric-pressure air *Plasma Phys. Rep.* **36** 90–8

[12] Stepanyan S, Soloviev V and Starikovskaia S 2014 An electric field in nanosecond surface dielectric barrier discharge at different polarities of the high voltage pulse: spectroscopy measurements and numerical modeling, *J. Phys. D: Appl. Phys.* **47** 485201

[13] Paris P, Aints M, Valk F, Plank T, Haljaste A, Kozlov K and Wagner H 2005 Intensity ratio of spectral bands of nitrogen as a measure of electric field strength in plasmas *J. Phys. D: Appl. Phys.* **38** 3894

[14] Paris P, Aints M and Valk F 2009 Collisional quenching rates of $N_2^+(B\ ^2\Sigma_g^+,\ v = 0)$ *Book of Contributed Papers of XVII Symposium on Application of Plasma Processes and Visegrad Workshop on Research of Plasma Physics* (Slovakia: University of Bratislava) pp 227–8

[15] Simeni M S, Goldberg B M, Zhang C, Frederickson K, Lempert W R and Adamovich I V 2017 Electric field measurements in a nanosecond pulse discharge in atmospheric air *J. Phys. D: Appl. Phys.* **50** 184002

[16] Boeuf J and Pitchford L 2005 Electrohydrodynamic force and aerodynamic flow acceleration in surface dielectric barrier discharge *J. Appl. Phys.* **97** 103307

[17] Likhanskii A V, Shneider M N, Macheret S O and Miles R B 2007 Modeling of dielectric barrier discharge plasma actuators driven by repetitive nanosecond pulses *Phys. Plasmas* **14** 073501

[18] Gibalov V I and Pietsch G J 2012 Dynamics of dielectric barrier discharges in different arrangements *Plasma Sources Sci. Technol.* **21** 024010

[19] Solovev V, Konchakov A, Krivtsov V and Aleksandrov N 2008 Numerical simulation of a surface barrier discharge in air *Plasma Phys. Rep.* **34** 594–608

[20] Soloviev V and Krivtsov V 2009 Surface barrier discharge modelling for aerodynamic applications *J. Phys. D: Appl. Phys.* **42** 125208

[21] Soloviev V and Krivtsov V 2014 Mechanism of streamer stopping in a surface dielectric barrier discharge *Plasma Phys. Rep.* **40** 65–77

[22] Soloviev V, Krivtsov V, Shcherbanev S and Starikovskaia S 2016 Evolution of nanosecond surface dielectric barrier discharge for negative polarity of a voltage pulse *Plasma Sources Sci. Technol.* **26** 014001

[23] Leonov S B, Petrishchev V and Adamovich I V 2014 Dynamics of energy coupling and thermalization in barrier discharges over dielectric and weakly conducting surfaces on μs to ms time scales *J. Phys. D: Appl. Phys.* **47** 465201

[24] Babaeva N Y, Tereshonok D V and Naidis G V 2016 Fluid and hybrid modeling of nanosecond surface discharges: effect of polarity and secondary electrons emission *Plasma Sources Sci. Technol.* **25** 044008

[25] Klochko A V, Starikovskaia S M, Xiong Z and Kushner M J 2014 Investigation of capillary nanosecond discharges in air at moderate pressure: comparison of experiments and 2D numerical modelling *J. Phys. D: Appl. Phys.* **47** 365202

[26] Anikin N, Starikovskaia S and Starikovskii A Y 2004 Study of the oxidation of alkanes in their mixtures with oxygen and air under the action of a pulsed volume nanosecond discharge *Plasma Phys. Rep.* **30** 1028–42

[27] Pancheshnyi S, Nudnova M and Starikovskii A 2005 Development of a cathode-directed streamer discharge in air at different pressures: experiment and comparison with direct numerical simulation *Phys. Rev.* E **71** 016407

[28] Popov N 2011 Fast gas heating in a nitrogen-oxygen discharge plasma: I. Kinetic mechanism *J. Phys. D: Appl. Phys.* **44** 285201

[29] Zhelezniak M, Mnatsakanian A K and Sizykh S V 1982 Photoionization of nitrogen and oxygen mixtures by radiation from a gas discharge *High Temp. Sci.* **20** 423–8

[30] Bourdon A, Pasko V, Liu N, Célestin S, Ségur P and Marode E 2007 Efficient models for photoionization produced by non-thermal gas discharges in air based on radiative transfer and the Helmholtz equations *Plasma Sources Sci. Technol.* **16** 656

[31] Luque A, Ebert U, Montijn C and Hundsdorfer W 2007 Photoionization in negative streamers: fast computations and two propagation modes *Appl. Phys. Lett.* **90** 081501

[32] Sonneveld P 1989 CGS, a fast lanczos-type solver for nonsymmetric linear systems *SIAM J. Sci. Stat. Comput.* **10** 36–52

[33] Schenk O and Gärtner K 2004 Solving unsymmetric sparse systems of linear equations with PARDISO *Future Gener. Comput. Syst.* **20** 475–87

[34] Ventzek P L, Sommerer T J, Hoekstra R J and Kushner M J 1993 Two-dimensional hybrid model of inductively coupled plasma sources for etching *Appl. Phys. Lett.* **63** 605–7

[35] Villa A, Barbieri L, Gondola M and Malgesini R 2013 An asymptotic preserving scheme for the streamer simulation *J. Comput. Phys.* **242** 86–102

[36] Li J-G 2008 Upstream nonoscillatory advection schemes *Mon. Weather Rev.* **136** 4709–29

[37] Verwer J G, Sommeijer B P and Hundsdorfer W 2004 RKC time-stepping for advection-diffusion-reaction problems *J. Comput. Phys.* **201** 61–79

[38] Zha G-C and Bilgen E 1993 Numerical solutions of euler equations by using a new flux vector splitting scheme *Int. J. Numer. Methods Fluids* **17** 115–44

[39] Vitello P, Penetrante B and Bardsley J 1994 Simulation of negative-streamer dynamics in nitrogen *Phys. Rev.* E **49** 5574

[40] Kulikovsky A 1998 Positive streamer in a weak field in air: A moving avalanche-to-streamer transition *Phys. Rev.* E **57** 7066

[41] Tardiveau P, Moreau N, Bentaleb S, Postel C and Pasquiers S 2009 Diffuse mode and diffuse-to-filamentary transition in a high pressure nanosecond scale corona discharge under high voltage *J. Phys. D: Appl. Phys.* **42** 175202

[42] Unfer T and Boeuf J 2009 Modelling of a nanosecond surface discharge actuator *J. Phys. D: Appl. Phys.* **42** 194017

[43] Pachuilo M V *et al* 2017 Dynamics of surface streamer plasmas at atmospheric pressure: mixtures of argon and methane *IEEE Trans. Plasma Sci.* **45** 1776–87

[44] Dubinova A, Trienekens D, Ebert U, Nijdam S and Christen T 2016 Pulsed positive discharges in air at moderate pressures

near a dielectric rod *Plasma Sources Sci. Technol.* **25** 055021

[45] Pechereau F, Jánsky J and Bourdon A 2012 Simulation of the reignition of a discharge behind a dielectric layer in air at atmospheric pressure *Plasma Sources Sci. Technol.* **21** 055011

[46] Pancheshnyi S, Starikovskaia S and Starikovskii A Y 1998 Measurements of rate constants of the $N_2(C^3\Pi_u, v = 0)$ and $N_2^+(B^2\Sigma_g^+, v = 0)$ deactivation by N_2, O_2, H_2, CO and H_2O molecules in afterglow of the nanosecond discharge *Chem. Phys. Lett.* **294** 523–7

[47] Stepanyan S, Starikovskiy A Y, Popov N and Starikovskaia S 2014 A nanosecond surface dielectric barrier discharge in air at high pressures and different polarities of applied pulses: transition to filamentary mode *Plasma Sources Sci. Technol.* **23** 045003

[48] Raizer Y P 1991 Gas discharge physics

[49] Viehland L and Mason E 1995 Transport properties of gaseous ions over a wide energy range, IV *At. Data Nucl. Data Tables* **60** 37–95

[50] Inada Y, Matsuoka S, Kumada A, Ikeda H and Hidaka K 2012 Shack-Hartmann type laser wavefront sensor for measuring two-dimensional electron density distribution over extinguishing arc discharge *J. Phys. D: Appl. Phys.* **45** 435202

[51] Radtsig A and Smirnov B 1980 *Handbook on Atomic and Molecular Physics* (Moscow: Atomizdat)

[52] Gordiets B, Osipov A I, Stupochenko E and Shelepin L A 1973 Vibrational relaxation in gases and molecular lasers *Phys.-Usp.* **15** 759–85

[53] Gaitonde D and McCrink M 2012 A semi-empirical model of a nanosecond pulsed plasma actuator for flow control simulations with LES *50th AIAA Aerospace Sciences Meeting including the New Horizons Forum and Aerospace Exposition* **184**

[54] Takashima K, Zuzeek Y, Lempert W R and Adamovich I V 2011 Characterization of a surface dielectric barrier discharge plasma sustained by repetitive nanosecond pulses *Plasma Sources Sci. Technol.* **20** 055009

[55] Zhu Y, Wu Y, Cui W, Li Y and Jia M 2013 Modelling of plasma aerodynamic actuation driven by nanosecond SDBD discharge *J. Phys. D: Appl. Phys.* **46** 355205

[56] Anokhin E, Kuzmenko D, Kindysheva S, Soloviev V and Aleksandrov N 2015 Ignition of hydrocarbon: air mixtures by a nanosecond surface dielectric barrier discharge *Plasma Sources Sci. Technol.* **24** 045014

[57] Benard N, Zouzou N, Claverie A, Sotton J and Moreau E 2012 Optical visualization and electrical characterization of fast-rising pulsed dielectric barrier discharge for airflow control applications *J. Appl. Phys.* **111** 033303